Di Sanzo, Spengler, *et al.*

1 **Mapping sites of carboxymethyllysine modification on proteins**

2 **reveals its consequences for proteostasis and cell proliferation**

3

4 **Authors:**

5 Simone Di Sanzo[1]*, Katrin Spengler[2]*, Anja Leheis[2], Joanna M. Kirkpatrick[1,5], Theresa L.

6 Rändler[2], Tim Baldensperger[3], Luca Parca[4], Christian Marx[1], Zhao-Qi Wang[1,6], Marcus A.

7 Glomb[3], Alessandro Ori[1]§# and Regine Heller[2]§#$

8

9 [1] Leibniz Institute on Aging – Fritz Lipmann Institute (FLI), 07745 Jena, Germany

10 [2] Institute of Molecular Cell Biology, Center for Molecular Biomedicine, Jena University Hospital, 07743 Jena, Germany

11 [3] Institute of Chemistry, Food Chemistry, Martin-Luther-University Halle-Wittenberg, 06120, Halle/Saale, Germany

12 [4] Bioinformatics Unit, IRCCS Casa Sollievo della Sofferenza, S. Giovanni Rotondo, Italy

13 [5] Current address: Proteomics Science Technology Platform, The Francis Crick Institute, MW1 1AT London, UK

14 [6] Faculty of Biological Sciences, Friedrich-Schiller-University of Jena, Jena, Germany

15

16

17 * These authors contributed equally to this work.

18 § These authors jointly supervised this work.

19 # Correspondence should be addressed to: alessandro.ori@leibniz-fli.de or regine.heller@med.uni-jena.de

20 $ Lead contact

21

22 **Summary**

23 Posttranslational mechanisms play a key role in modifying the abundance and function of cellular

24 proteins. Among these, modification by advanced glycation end products (AGEs) has been shown

25 to accumulate during aging and age-associated diseases but specific protein targets and

26 functional consequences remain largely unexplored. Here, we devised a proteomic strategy to

27 identify specific sites of carboxymethyllysine (CML) modification, one of the most abundant AGEs.

28 We identified over 1000 sites of CML modification in mouse and primary human cells treated with

29 the glycating agent glyoxal. By using quantitative proteomics, we found that protein glycation

30 triggers a proteotoxic response and directly affects the protein degradation machinery. We show

31 that glyoxal induces cell cycle perturbation in primary endothelial cells and that CML modification

32 reduces acetylation of tubulins and impairs microtubule dynamics. Our data demonstrate the

33 relevance of AGE modification for cellular function and pinpoint specific protein networks that

34 might become compromised during aging.

Di Sanzo, Spengler, *et al.*

1

Keywords: advanced glycation end products; carboxymethyllysine; posttranslational modification; aging; proteasome; endothelial cell; cell cycle; tubulin; acetylation; mass spectrometry

Highlights

- A peptide enrichment strategy allows mapping of CML modification in cells and tissues
- CML modification competes with ubiquitination or acetylation of lysines
- Glyoxal treatment destabilizes the 26S proteasome
- Glyoxal arrests cell cycle and impairs microtubule dynamics via altering the tubulin code

Introduction

Advanced glycation end products (AGEs) are generated via a non-enzymatic glycation of proteins initiated by the reaction of glucose, fructose or highly reactive dicarbonyls such as methylglyoxal or glyoxal with amino acids (Brownlee, 1995). Glycation is enhanced when glucose levels are high, when dicarbonyls deriving from glycolytic intermediates or lipid peroxidation accumulate (Nigro et al., 2019), or when dicarbonyl detoxification by glyoxalases such as glyoxalase 1 (GLO1) and protein deglycase DJ-1 is low (Nigro et al., 2017). AGE formation may alter structure and function of the targeted proteins and, in addition, AGEs may elicit their effects as ligands of the pro-inflammatory receptor for advanced glycation end products (RAGE) (Teissier and Boulanger, 2019). One of the most abundant AGEs *in vivo* is N(6)-carboxymethyllysine (CML), whose formation is triggered, among other routes, by glyoxal (Brings et al., 2017). CML is known to be chemically stable, to accumulate in human tissues in diabetes, atherosclerosis, neurodegeneration and aging, and thus to be a biomarker of aging (Delgado-Andrade, 2016).

A causal relationship between the buildup of AGEs and individual disease is still under debate, but studies in which AGE levels were modulated via the GLO1 system, provided first evidence. Overexpression of GLO1 increases lifespan in *C. elegans* (Morcos et al., 2008) and reduces endothelial dysfunction in diabetic mice (Brouwers et al., 2014), while knockdown of GLO1 mimics diabetic nephropathy in non-diabetic mice (Giacco et al., 2014). Glycation of extracellular proteins such as hemoglobin HbA1c (Shapiro et al., 1980) or collagen (Avery and Bailey, 2005) is well described, but reports on glycation of intracellular proteins are still scarce. Examples of those are histones (Ansari et al., 2018; Baldensperger et al., 2020; Galligan et al., 2018; Guedes et al., 2011; Mir et al., 2014; Zheng et al., 2019; Zheng et al., 2020), mitochondrial proteins (Hamelin et al., 2007; Rosca et al., 2005; Wang et al., 2009), the 20S proteasome (Queisser et al., 2010),

Di Sanzo, Spengler, *et al.*

1 enzymes involved in energy production (Snow et al., 2007), small heat shock proteins (Oya-Ito et

2 al., 2006; Schalkwijk et al., 2006; Sudnitsyna and Gusev, 2017) and the sodium channel Nav1.8

3 (Bierhaus et al., 2012). Glycation is increasingly seen as a driver of metabolic disease and aging,

4 and it may elicit specific effects by targeting signaling proteins (Chaudhuri et al., 2018; Kold-

5 Christensen and Johannsen, 2020). In this context, glycation of the ryanodine receptor associated

6 with successive Ca^{2+} leakage and mitochondrial damage (Ruiz-Meana et al., 2019), reversible

7 inhibitory glycation of nuclear factor erythroid 2-related factor 2 (Nrf2) (Sanghvi et al., 2019), and

8 methylglyoxal-induced dimerization of Kelch-like ECH-associated protein 1 (KEAP1) with

9 subsequent activation of the KEAP1/Nrf2 transcriptional program (Bollong et al., 2018) have been

10 reported. The latter may play a role in the upregulation of defense systems, such as GLO1 and

11 the ubiquitin-proteasome system (UPS), and may be involved in the hormetic effect of

12 methylglyoxal (Ravichandran et al., 2018). In contrast to earlier assumptions of irreversible AGE

13 formation, recent studies suggested the possibility of deglycation via DJ-1 or protein arginine

14 deiminase 4 (Zheng et al., 2019; Zheng et al., 2020).

15 A global characterization of the targeted proteins and pathways, which may significantly contribute

16 to manifestation of metabolic diseases and aging, is a prerequisite to further understand

17 pathophysiological effects of AGEs, like CML. Here, we developed a proteomic workflow based

18 on selective enrichment of CML-modified peptides coupled to mass spectrometry for identification

19 and quantification. We applied this approach to two cellular models (mouse embryonic fibroblasts

20 (MEF) and human umbilical vein endothelial cells (HUVEC)), and to tissues of young and

21 chronologically aged mice. This strategy allowed us to identify specific sites of CML modification.

22 We show that CML modification of proteins competes with ubiquitination or acetylation, and that

23 it destabilizes components of the UPS. CML accumulation in primary endothelial cells led to

24 inhibition of proliferation, which was due to both altered expression of cell cycle regulators, and

25 glycation of tubulins associated with impaired microtubule dynamics.

26 **Results**

27 *An enrichment strategy for the identification of CML-modified peptides*

28 Aiming to identify sites of CML modification on proteins, we developed a proteomic workflow

29 employing an antibody-based enrichment of CML-modified peptides coupled to mass

30 spectrometry (CMLpepIP). We applied CMLpepIP to MEF and HUVEC treated with different

31 concentrations of glyoxal, a cell-permeable dialdehyde (Fig. 1A). In both cell types, glyoxal

32 treatment led to a dose-dependent increase of total CML levels, as verified by immunoblot (Fig.

1   1B), and amino acid absolute quantification using liquid chromatography mass spectrometry (LC-

2   MS) (Fig. 1C). To assess the efficiency of our enrichment protocol, we compared the fraction of

3   peptide spectrum matches (PSM) assigned to CML-containing peptides between elutions from

4   the enriched and control samples. When CMLpepIP was applied to glyoxal-treated cells, we

5   achieved up to 7 times more PSM from CML-containing peptides as compared to controls. With

6   a lower concentration of glyoxal, the gain of modified peptides was reduced and, in any case, the

7   fraction of PSM assigned to CML peptides never exceeded 5% (Fig. 1D). This indicates that

8   CMLpepIP enables reproducible (Fig. S1A and S1B), but only partial, enrichment of CML-modified

9   peptides, especially in high complexity samples where CML peptides occur at low concentration

10   (<1%).

11   Using CMLpepIP, we identified 995 unique CML sites in MEF and 451 in HUVEC of which 941,

12   and 330 were deemed 'highly confident', respectively (see Methods for applied cut-offs) (Fig. S1A

13   and Table S1). Overlapping sets of CML sites were reproducibly identified across conditions and

14   independent experiments (Fig. S1B and S1C). To validate the identified CML peptides, we

15   performed parallel reaction monitoring (PRM) measurements using isotopically labeled spike-in

16   peptide standards derived from our list of identified CML sites (Table S1). Co-elution of

17   endogenous (light) and standard (heavy) peptides validated the identified CML-modified peptides,

18   and it enabled quantitation relative to the spike-in standard across conditions that recapitulated

19   the absolute levels of CML measured by LC-MS (Fig. 1E,F).

20   A subset of conserved CML sites was found to be modified in both MEF and HUVEC (Fig. 1G).

21   These sites localized on proteins involved in translation, RNA binding and chromatin remodeling

22   at the centromere as well as on structural constituents of the cytoskeleton and mitochondrial

23   proteins (Fig. 1H and Table S1). Since long-lived proteins are postulated to be the main targets

24   of AGEs (Gkogkolou and Bohm, 2012; Smuda et al., 2015; Verzijl et al., 2000), we used published

25   turnover data (Mathieson et al., 2018) and investigated the turnover distribution for modified and

26   non-modified proteins in MEF and HUVEC. In both cell types, proteins with slower turnover were

27   more likely to be affected by CML modification, independently of their subcellular localization (Fig.

28   1I left - J left), indicating slow turnover as an important determinant of CML modification. Although

29   we were able to detect CML sites across the entire dynamic range of identified proteins in both

30   cell types (Fig. S1D), we noted that protein abundance correlated with CML modifications, with

31   high abundant proteins being more often detected as modified (Fig. 1I right - J right).

Di Sanzo, Spengler, *et al.*

1   Taken together, CMLpepIP enabled us to investigate the CML-modified proteome and to identify

2   specific and conserved targets of AGE-modification in two different primary culture systems.

3   Lower turnover and high abundance appear to be key factors in driving CML modification *in vitro*.
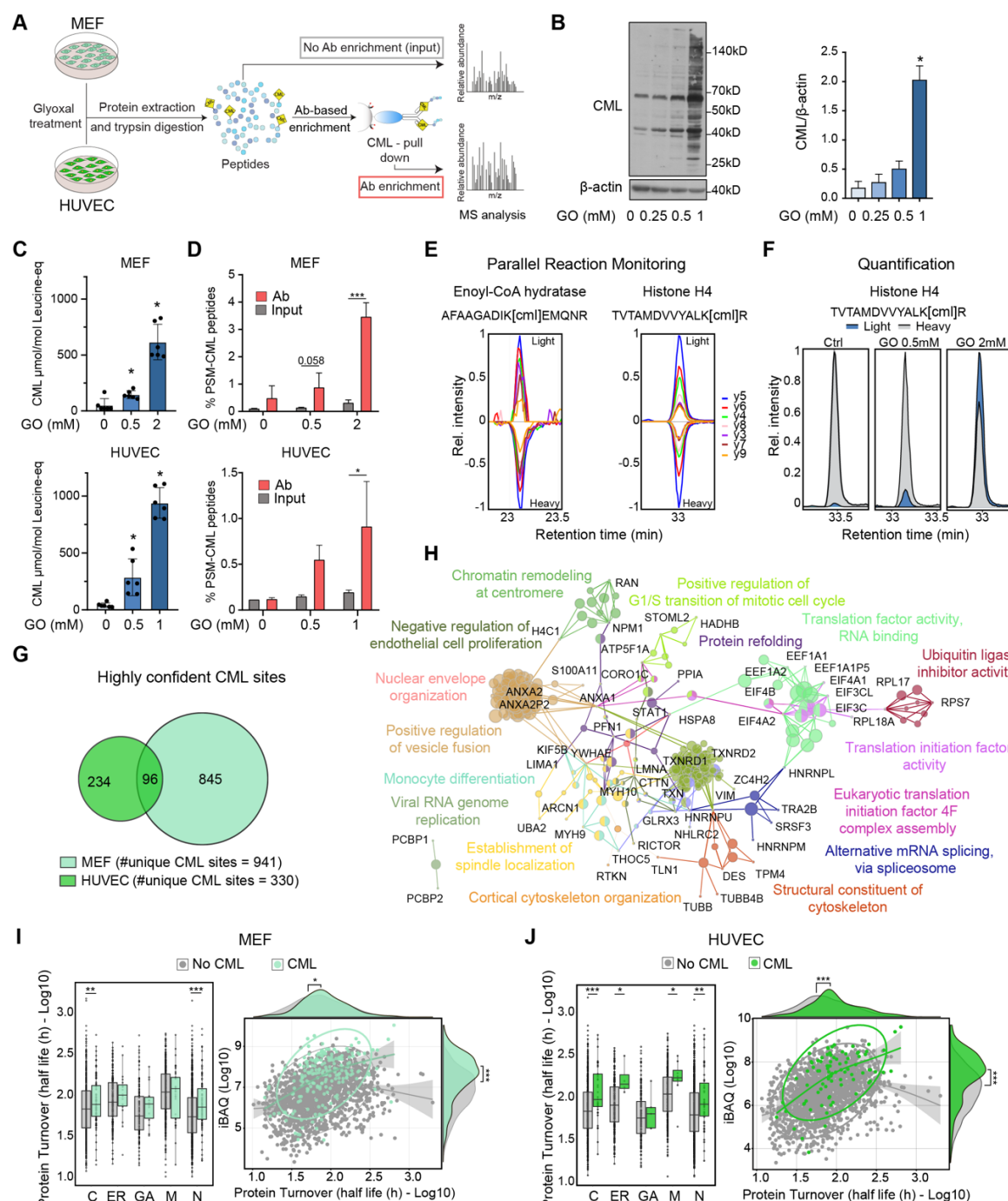

4

5   **Figure 1. Antibody-based enrichment of CML-modified peptides**.

6   **A.** Workflow for the identification of CML-modified peptides. Ab: antibody **B.** Immunoblot (left) and densitometry-based

7   quantification (right) for CML-modified proteins from HUVEC treated with glyoxal (GO) for 48 h. n=3, * p<0.05 vs.

8   control, one-way repeated measurement ANOVA corrected using Holm-Šidák method. **C.** Quantification of total CML

5

1 levels in MEF and HUVEC treated with GO for 8 h or 48 h, respectively. n=6, * p<0.05 vs. control, one-way ANOVA
2 using Geisser-Greenhouse correction. **D.** Percentage of peptide spectrum matches (PSM) containing CML modification
3 among different conditions. n=3 (MEF), n=2 (HUVEC), * p<0.05, *** p<0.001. Multiple t-test corrected using Holm-Šidák
4 method. **E.** Validation of CML-modified peptides by parallel reaction monitoring (PRM) using heavy spike-in peptides.
5 **F.** Quantification of a CML-modified peptide from histone H4 by PRM in MEF treated with GO for 24h. **G.** Venn diagram
6 showing the overlap between unique highly confident CML sites identified in MEF and HUVEC. **H.** Enrichment of Gene
7 Ontology biological processes among CML sites identified in both HUVEC and MEF. The enrichment was performed
8 using the Cytoscape App ClueGO. **I-J.** Left, protein turnover of CML-modified proteins grouped according to their
9 subcellular localization, as defined by Gene Ontology annotation. Turnover data were taken from (Mathieson et al.,
10 2018). C: cytoplasm; ER: endoplasmic reticulum; GA: Golgi apparatus; M: mitochondria; N: nucleus. Right, scatterplot
11 comparing protein abundance (iBAQ scores, averages of n=3 (MEF), n=2 (HUVEC)) and protein turnover of CML-
12 modified proteins. * p<0.05, ** p<0.01, *** p<0.001, Wilcoxon Rank Sum test with continuity correction. Related to Fig.
13 S1 and Table S1.

14

15 *Sites of CML modification in mouse organs*

16 Next, we applied CMLpepIP to investigate protein targets of CML *in vivo.* We analyzed heart,

17 kidney and liver from young (3-4 months) and geriatric C57BL/6J mice (26-33 months), and, in

18 parallel, age-related changes of protein abundance using quantitative MS (Fig. 2A). The selected

19 organs showed a higher basal level of total CML content compared to, e.g., brain (Fig. S2A). We

20 identified 257, 186 and 52 unique CML sites in heart, kidney and liver, respectively, of which 190,

21 142 and 34 were deemed 'highly confident', respectively (Table S2). Using PRM with spike-in

22 heavy peptides, we validated 16 (89%) out of those 18 CML sites, for which we had successfully

23 developed PRM assays (Fig. S2B-C). CML appeared to target proteins in an organ-specific

24 manner (Fig. 2B). The affected proteins participate in biological processes related to energy

25 production in the heart, cytoskeleton in the kidney, and detoxification in the liver (Fig. 2C). Similar

26 to what we observed in cultured cells (Fig. 1I,J), CML sites in the heart appeared to occur

27 preferentially in proteins with slow turnover (Fig. S2D). Since CML modification occurs on lysines

28 and these residues are targets for other posttranslational modifications (PTM), we assessed the

29 overlap of CML sites and other known PTM. We found that approximately one third of the

30 identified CML sites (97 out of 334 unique highly confident sites) occur on residues that are known

31 to be modified by other PTM, primarily ubiquitination and acetylation (Fig. 2D). These data

32 suggest that modification by CML might interfere with biological processes by impeding other

33 PTM to occur on specific residues.

34 We next investigated age-related changes of protein abundance in the same tissues using

35 Tandem Mass Tag (TMT)-10plex labeling (Fig. 2A). Principal component analysis could clearly

36 distinguish two different clusters formed by young and old mice for all the three organs (Fig. 2E).

1   By applying gene set enrichment analysis, we identified pathways affected by protein abundance

2   changes in aged organs (Fig. S2E). Among these, a pathway related to AGE signaling was

3   enriched with aging both in heart and kidney. This pathway included components of the fibrotic

4   process such as several types of collagen I and IV, but also proteins mediating signaling

5   downstream of extracellular AGEs via RAGE such as NFκB1, MAPK9 and AKT1. In addition, we

6   specifically queried the data for proteins involved in dicarbonyl detoxification via GLO1 and found

7   a general trend for a decreased abundance of the components of this network in all organs

8   isolated from geriatric mice (Fig. 2F). We validated the functional relevance of decreased GLO1

9   protein levels by confirming a decrease of its activity in old organs (Fig. 2G).

10 Inspired by this and by the well-established increase of total AGE levels in old tissue (Chaudhuri

11 et al., 2018; Delgado-Andrade, 2016; Nigro et al., 2019), we tested whether we could detect an

12 age-dependent elevation of CML modification at specific sites. Using PRM assays on total tissue

13 lysates, we demonstrated an age-dependent raise in the level of CML modification of histone H4

14 at position K92 that exceeded the abundance change observed at the protein level in heart and

15 kidney (Fig. 2H). However, no age-related changes in the levels of two other CML sites, i.e., K263

16 of adenine nucleotide translocase type 1 and K154 of ATP synthase subunit γ, were observed

17 (Fig. 2I).

18 Together, these data show that the targets of AGEs are organ-specific, and that the levels of CML

19 modification increase with aging in a site-specific manner, likely as a consequence of reduced

20 levels and activity of dicarbonyl-detoxifying enzymes in old organs.

Di Sanzo, Spengler, *et al.*

Figure 2. The CML-modified proteome in mouse organs.

A. Workflow for the analysis performed on mouse tissues from young (Y) and old (O) mice. Tandem Mass Tag (TMT) was used for monitoring protein abundance, CMLpepIP for CML site identification and PRM for CML site quantification. **B.** Venn diagram of highly confident CML sites identified in heart, kidney and liver. **C.** Enrichment of Gene Ontology biological processes among CML sites identified from heart, kidney and liver. The enrichment was performed using the

Di Sanzo, Spengler, *et al.*

1   Cytoscape App ClueGO. **D.** Overlap between CML sites and other PTM. The gray scale pie charts indicate the number
2   of CML sites overlapping with known PTM. The colored pie charts indicate which PTM class overlap with CML sites
3   (shown as percentages). Known PTM were obtained from Minguez et al., 2015; Hornbeck et al., 2015). **E.** Principal
4   component analysis of proteome data from young and old mice (n=5 per age group). The smaller dots represent
5   individual samples and the larger dots the centroids of each age-matched group. Ellipses represent 95% confidence
6   intervals. The percentage of variance explained by the first two principle components (PC) axes is reported in the axis
7   titles. **F.** Effect of aging on the abundance of proteins part of the glyoxalase 1 (GLO1) network. The network was
8   extracted from https://string-db.org using input GLO1. n=5, * adj. p<0.05, ** adj. p<0.01, *** adj. p<0.001, t-test with
9   Benjamini-Hochberg correction for multiple testing, as implemented in *limma*. **G.** GLO1 activity tested on heart, kidney
10   and liver lysates from young (Y) and old (O) mice. n=7, * p<0.05, *** p<0.001, unpaired t-test, parametric, two-tailed.
11   **H-I.** Normalized protein intensity of histone H4, ADP/ATP translocase type 1 and ATP synthase subunit γ from TMT
12   experiment (Protein - left panel) and intensity of CML-modified peptides from PRM (right panel). n=5 for protein
13   abundance, n=8 for CML-modified peptides, * p<0.05, *** p<0.001, **** p<0.0001, unpaired t-test. Related to Fig. S2
14   and Table S2.

15

16   *CML modification directly targets the ubiquitin-proteasome system*

17   To better understand the consequences of increased CML modifications in tissues, we performed

18   experiments to characterize cellular functions in response to glyoxal treatment. Since we

19   observed that some of the CML targets are proteins involved in protein quality control (Fig. S3A),

20   we hypothesized that accumulation of glyoxal impairs proteostasis and triggers cellular responses

21   to counteract proteotoxic stress. To address this question, we applied a data-independent

22   acquisition (DIA) method to monitor proteome-wide changes of protein abundance in MEF treated

23   with different glyoxal concentration for 8 h and 24 h (Fig. 3A and S3B). Short treatment (8 h) with

24   0.5 mM and 2 mM glyoxal induced only few significant changes of protein abundance, however,

25   a longer treatment (24 h) triggered a major proteome response that was dose-dependent (Fig.

26   3B). At this time point, the abundance of CML-modified proteins was significantly increased (Fig.

27   3C), while KEGG pathways related to the UPS, especially ubiquitin-conjugating enzymes (E2),

28   were decreased (Fig. 3D and S3C).

29   Interestingly, we found a significant increase of components of the 26S proteasome induced by

30   glyoxal treatment in a dose-dependent manner in both MEF and HUVEC (Fig. 3E left and S3D).

31   However, while 0.5 mM glyoxal also increased proteasomal activity in MEF, the induction of 26S

32   proteasome by 2 mM glyoxal was not followed by a corresponding increase of activity (Fig. 3E

33   right). In parallel, we observed a dose-dependent accumulation of ubiquitinated proteins 24 h after

34   glyoxal treatment (Fig. 3F). We speculated that the lack of proteasome activity increase at high

35   doses of glyoxal might be due to a functional impairment of the proteasome itself. To test this, we

36   evaluated the thermal stability of proteasomal proteins in MEF treated with glyoxal using thermal

37   proteome profiling (Franken et al., 2015). This analysis revealed that glyoxal treatment negatively

38   impacted the thermal stability of most of the 26S proteasome subunits in a dose-dependent

Di Sanzo, Spengler, *et al.*

1 fashion (Fig. 3G), while the overall thermal stability of proteins remained comparable across the

2 tested conditions (Fig. S3E and Table S3). In addition, we identified a subset of proteasomal

3 proteins and other members of the UPS, including ubiquitin itself, to be directly CML-modified

4 both in cells treated with glyoxal and in organs (Fig. S3A).

5 Taken together these data describe a specific and dose-dependent proteome response to glyoxal

6 exposure. This is characterized by accumulation of CML-modified proteins and an induction of

7 compensatory mechanisms including the UPS. The UPS may become saturated at higher glyoxal

8 concentration due to the accumulation of CML-modified and ubiquitinated proteins, and to a

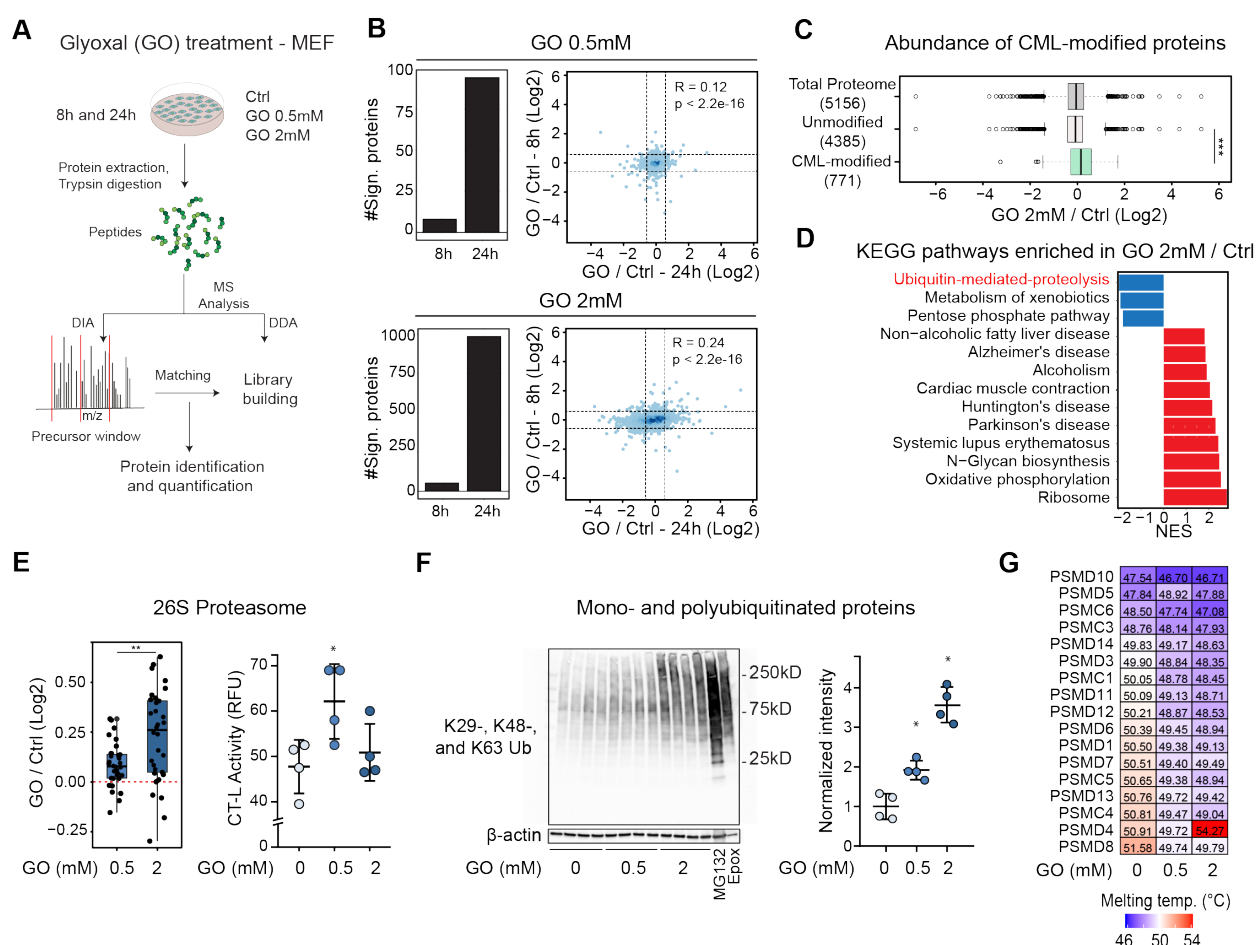9 destabilization of the 26S proteasome.

10

11 **Figure 3**. **The proteome response to glyoxal (GO) treatment**.

12 **A.** Workflow for the analysis of proteome changes induced in MEF by GO. **B.** Left, number of significant proteins

13 (absolute log2 fold change>0.58 and q<0.05) after 8 and 24 h GO treatment. Right, scatterplots comparing the log2

14 fold changes induced by GO at 8 or 24 h. Dashed lines represent the log2 fold change cut-offs used (±0.58). n=5 (8 h),

15 n=4 (24 h). **C.** Distribution of protein fold changes for 2 mM GO vs. control (Ctrl) after 24 h of treatment. Average values

16 of n=4 were compared, *** p<0.001, Wilcoxon rank sum test continuity correction with alternative two-sided. **D.** Gene

17 Set Enrichment Analysis (GSEA) for KEGG pathways based on protein fold changes induced by 2 mM GO after 24 h

10

Di Sanzo, Spengler, *et al.*

1   of treatment. Normalized enrichment score (NES) indicates pathways enriched among proteins that increase (red) or
2   decrease (blue) upon GO treatment (FDR<0.05). All the proteins quantified were ranked according to their log2 fold
3   change and used as input for GSEA. **E.** Boxplot of fold changes for members of the 26S proteasome (left) and
4   proteasome chymotrypsin-like (CT-L) activity (right) in MEF treated with GO for 24 h compared to Ctrl. n=4, ** p<0.01,
5   Wilcoxon Rank Sum test with continuity correction. **F.** Immunoblot for mono- and polyubiquitinated proteins from MEF
6   lysates treated with GO for 24 h. Lysates from cells treated with proteasome inhibitors MG132 (20 µM for 6h) or
7   epoxomicin (Epox, 10 nM for 96h) were loaded as positive controls. n=4, * p<0.05, one-way ANOVA using Geisser-
8   Greenhouse correction. **G.** Heatmap representing the melting point temperature of members of 26S proteasome
9   identified in all conditions obtained using thermal proteome profiling. Related to Fig. S3 and Table S3.

10

11   *Glyoxal inhibits proliferation of primary human endothelial cells by inducing cell cycle arrest and*
12   *inhibiting microtubule dynamics*

13   In endothelial cells, glyoxal-induced CML modifications occurred mainly in proteins of the nucleus,
14   the cytoskeleton and the mitochondria (Fig. 4A and Table S4), while glyoxal-initiated changes in
15   protein abundance comprised an upregulation of stress response proteins, e.g., heme oxygenase
16   1, and a downregulation of processes related to proliferation and growth (Fig. 4B). In particular,
17   several factors involved in DNA replication were downregulated. This was also reflected on a
18   functional level since glyoxal led to an inhibition of endothelial cell proliferation as demonstrated
19   by reduced cell numbers and lower incorporation of BrdU in the presence of serum or after
20   stimulation with basic fibroblast growth factor (bFGF) (Fig. 4C,D). Furthermore, angiogenic
21   sprouting in response to vascular endothelial growth factor (VEGF) was impaired (Fig. 4E).
22   Glyoxal-treated cells did not show signs of apoptosis (Fig. S4A).

23   Since mitochondrial proteins, e.g., ATP synthase subunit γ, were found to be CML-modified (Fig.
24   1H), we asked whether alterations in cellular energy production would underlie the observed
25   inhibition of cell proliferation. Seahorse analyses revealed a decrease in basal respiration and
26   mitochondrial ATP production in HUVEC treated with glyoxal (1 mM, 48 h) (Fig. 4F and Fig. S4B)
27   as well as an upregulation of glycolysis (Fig. 4G and Fig. S4C). The latter, together with an
28   increased mitochondrial biogenesis (Fig. 4H), likely compensated the reduction of mitochondrial
29   ATP production, since total cellular ATP was not altered (Fig. 4I). These data show that the cellular
30   energy homeostasis was maintained despite the exposure of cells to dicarbonyl stress and that
31   reduced cell proliferation was not due to metabolic limitations.
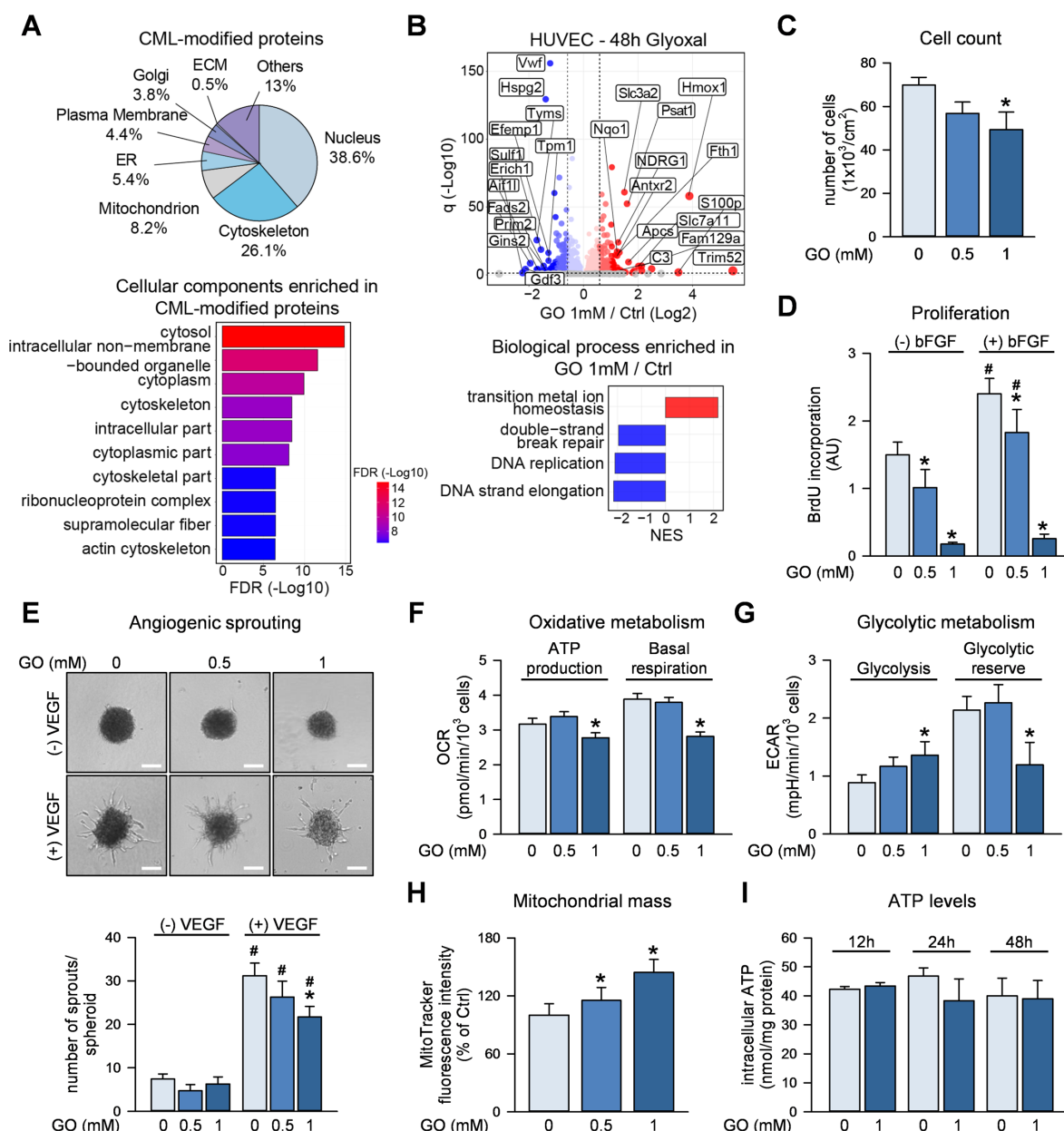
32

Di Sanzo, Spengler, *et al.*

Figure 4. Glyoxal (GO) impairs the proliferation of HUVEC.
A. Upper panel: CML-modified proteins annotated to different cellular compartments according to Gene Ontology annotation after GO treatment (1 mM, 48 h). Lower panel: Gene Ontology cellular component terms enriched in CML-modified proteins. False Discovery Rate (FDR) <0.05. **B.** Upper panel: volcano plot depicting proteins that significantly increase (red) or decrease (blue) abundance upon GO treatment (1 mM, 48 h) or remain unchanged (gray). Horizontal dashed line indicates a significance cut-off of q<0.05 and vertical dashed lines an absolute fold change (log2)>0.58. Lower panel: gene set enrichment analysis for Gene Ontology biological process terms based on protein fold changes. Terms enriched among increased (red) or decreased (blue) proteins are shown. FDR<0.05; NES: normalized enrichment score. **C-H**. HUVEC were treated with GO for 48 h. **C**. Cell numbers were determined. n=5. **D**. Cells were stimulated with bFGF (50 ng/ml, 24 h) and BrdU incorporation was measured. n=5. **E**. Spheroids were generated, embedded and stimulated with VEGF (50 ng/ml, 24 h). Representative pictures and sprout numbers per spheroid are shown. Scale bar=100 µm. n=4. **F-G**. Oxygen consumption rate (OCR) (**F**) and extracellular acidification rates (ECAR)

1   (**G**) were measured via Seahorse technology and mitochondrial and glycolytic parameters calculated. n=6. **H**. Cells
2   were stained with MitoTracker and analyzed by flow cytometry. n=5. **I**. HUVEC were treated with 1 mM GO and
3   intracellular ATP levels were measured in cell extracts. n=3. **C-I**. Data are represented as mean ± SEM. Statistical
4   significance was analyzed using one-way or two-way repeated measurement ANOVA corrected using Holm-Šidák
5   method. * p<0.05 vs. control, # p<0.05 vs. respective non-bFGF or non-VEGF-treated sample. Related to Fig. S4 and
6   Table S4.

7   To further clarify the mechanisms underlying inhibition of cell proliferation by glyoxal, we analyzed

8   its effect on the cell cycle. Applying a triple staining method, we found that treating endothelial

9   cells with glyoxal for 24 h triggered an arrest in G0/G1 and G2 phases, while the percentage of

10 cells in the S and M phases was significantly decreased (Fig. 5A). Some of these alterations,

11 especially the decrease in mitosis, were already seen after 4 h of glyoxal treatment, although at

12 a lower degree. In accordance with the lower entry of cells into S and M phases, we observed a

13 decrease of the cell cycle markers cyclin A (S phase) and phosphorylated H3(S10) (p-H3(S10),

14 M phase) (Fig. S5A). In addition, tracking cell proliferation dynamics revealed a slower

15 proliferation in response to the high dose of glyoxal (Fig. 5B).

16 We hypothesized that the observed cell cycle arrest induced by glyoxal was due to altered

17 expression of cell cycle regulators plus to specific glycation of proteins involved in cell cycle

18 control, which were both identified in glyoxal-treated cells (Fig. 5C). Interestingly, alteration of

19 protein expression was mainly related to proteins involved in the regulation of S and G1 phases,

20 while glycation was mostly observed in proteins controlling G2 and M phases, for instance, in

21 tubulin α and β chains (Fig. 5C). Strikingly, 8 out of 10 subunits of the replicative helicase MCM2-

22 7/GINS/CDC45 and several factors involved in lagging strand DNA synthesis such as subunits of

23 DNA polymerases α and δ, FEN1 and DNA ligase 1 were downregulated, whereas the cyclin-

24 dependent kinase inhibitor 1A (CDKN1A)/p21 was upregulated.

25 One pathway through which the expression of cell cycle regulators is affected is the DNA damage

26 response. Glyoxal triggered phosphorylation of the checkpoint kinase 1 (CHK1) and led to an

27 increased percentage of cells with γH2AX foci (Fig. 5D,E). As a consequence, and in line with the

28 proteomics data, the p53/p21 pathway was upregulated by glyoxal (Fig. 5F and S5B).

29 Immunoblotting experiments showed that especially with the higher dose of glyoxal the

30 abundance and, additionally, the phosphorylation of p53 as well as the expression of its target

31 CDKN1A/p21 increased. The expression of another inhibitor of cyclin-dependent kinases, p16,

32 was enhanced, too (Fig. 5F). We also found that after treatment with 1 mM glyoxal a small

33 proportion of cells (~12%) acquired a senescent phenotype, as shown by positive staining for

34 senescence-associated beta-galactosidase (SA-β-Gal) (Fig. S5C). This may be related to

Di Sanzo, Spengler, *et al.*

1 persistent dicarbonyl and oxidative stress since glyoxal led to increased mitochondrial and

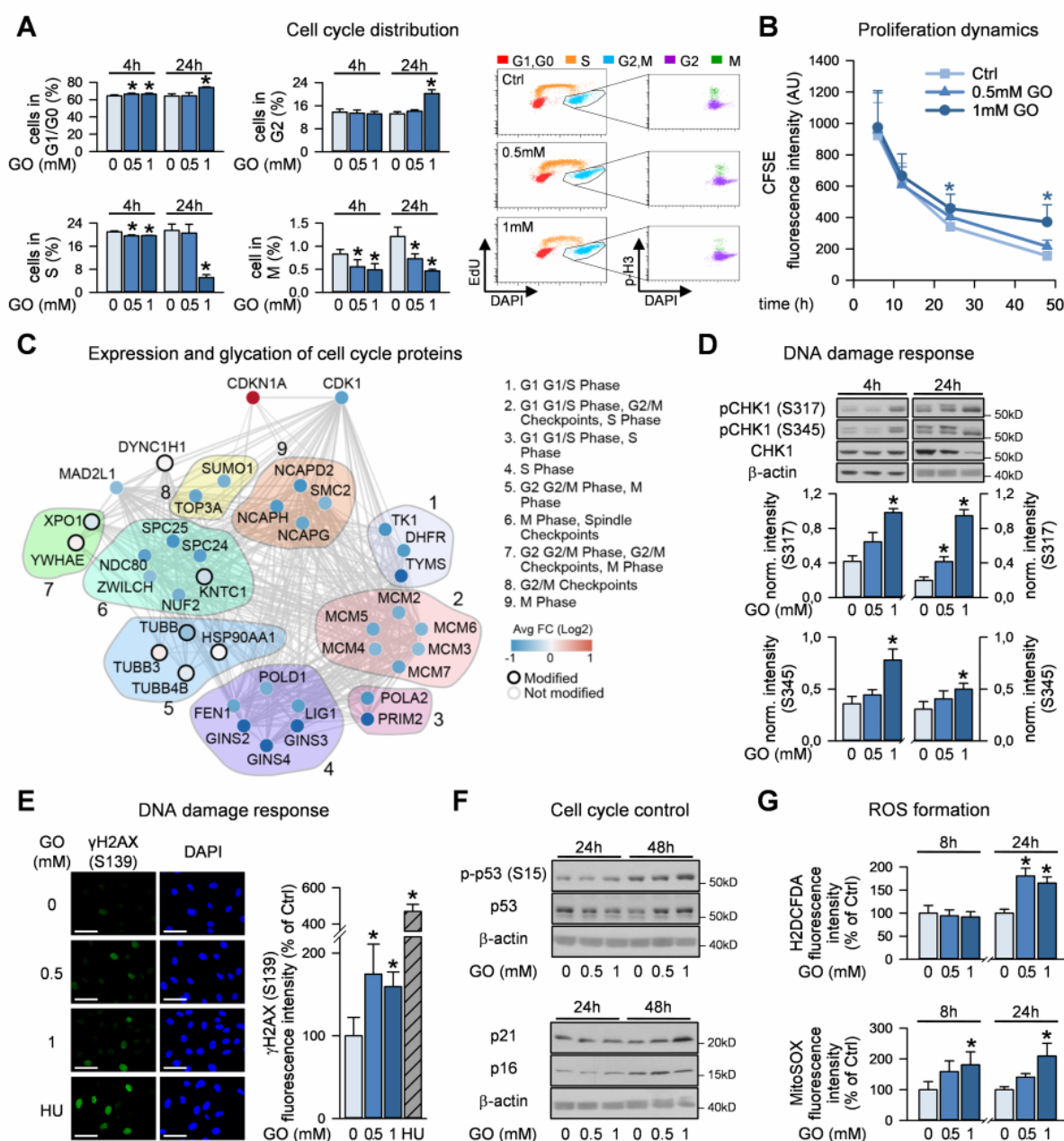2 cytosolic formation of reactive oxygen species (ROS) (Fig. 5G).

3

4 **Figure 5. Perturbation of the cell cycle induced by glyoxal (GO).**
5 **A**. HUVEC were treated with GO as indicated and subjected to cell cycle analysis applying a triple staining method
6 (EdU, p-H3 (S10), DAPI). Ratio of cells in the respective cell cycle phases (left) and representative dot plots (right) are
7 shown. n=4. **B**. HUVEC were stained with carboxyfluorescein succinimidyl ester (CFSE) and treated with GO. CFSE
8 staining was quantified by flow cytometry. n=4. **C**. Cell cycle proteins were chosen according to Reactome annotation
9 divided by their specific role in each phase. Only proteins with significantly altered expression (absolute fold
10 change>0.58 and q<0.05) or modified by CML are shown. Each dot represents the protein fold change and the black
11 edge signifies proven CML modification. **D**. GO-treated HUVEC were lysed and subjected to immunoblot analysis. n=5

14

1   (4 h), n=6 (24 h). **E**. Following GO treatment of HUVEC (8h), immunofluorescence staining of γH2AX (S139) and DAPI
2   was performed. Hydroxyurea (HU, 2 mM, 1 h) served as positive control. Representative pictures and quantification of
3   γH2AX (S139)-positive nuclei are shown. Scale bar=50 μm. n=3. **F**. HUVEC were treated with GO, lysed and subjected
4   to immunoblot analysis. Densitometric quantification is shown in figure S5B. n=6. **G**. HUVEC were treated with GO and
5   intracellular (H2DCFDA) and mitochondrial ROS (MitoSOX) were measured by flow cytometry. n=4. Statistical
6   significance was analyzed using one-way or two-way repeated measurement ANOVA corrected using Holm-Šidák
7   method. * $p < 0.05$ vs. respective control. Related to Fig. S5 and Table S5.

8   To understand how, on the other hand, glycation of proteins may affect cell cycle progression, we

9   focused on tubulins, which exhibited CML modification of different lysines upon glyoxal treatment

10 and in tissues from old mice (Fig. 6A and S6). CML-modified tubulin showed more strongly

11 structured tubulin filaments when compared to tubulin in control cells (Fig. 6B), and an increased

12 stability against the depolymerizing agent nocodazole (Fig. 6C). These data point to an

13 impairment of microtubule dynamics upon glyoxal treatment, which may affect mitosis and

14 contribute to the observed reduction of cell proliferation. To check this, we compared mitosis in

15 glyoxal-treated and control cells independent from G1 and G1/S transition. We performed a

16 double thymidine block to synchronize cells in early S phase, treated them with glyoxal thereafter

17 and monitored time-dependent expression of the mitotic marker p-H3(S10) in immunoblotting

18 experiments. In control cells, p-H3(S10) signals were detected between 16 h and 18 h after

19 releasing the cell cycle block, while glyoxal-treated cells showed reduced intensity of p-H3(S10)

20 signals indicating a lower number of mitotic cells (Fig. 6D).

21 CML modification of tubulin may directly affect microtubule dynamics but may also compete with

22 other lysine modifications, thereby affecting tubulin functionality. Since the lysine residues of

23 tubulin, which are modified by CML, are also known to be acetylated (Sadoul and Khochbin, 2016)

24 (Fig. 6A), we hypothesized that CML modification may impede tubulin acetylation. Indeed, glyoxal

25 treatment of HUVEC led to reduced tubulin acetylation at lysine 40 (K40) (Fig. 6E-F), which is

26 known to protect microtubules from mechanical damage and to facilitate self-repair (Portran et

27 al., 2017; Xu et al., 2017). Of note, we were able to demonstrate a direct competition of CML

28 modification and acetylation at K58 of the tubulin β-4B chain in glyoxal-treated cells. Glyoxal

29 induced a significant CML modification of K58 and at the same time, K58 acetylation was reduced

30 (Fig. 6G). Together, these data suggest that CML modification of tubulin is likely to have an impact

31 on acetylation and may thereby affect its interactions with microtubule-binding proteins and
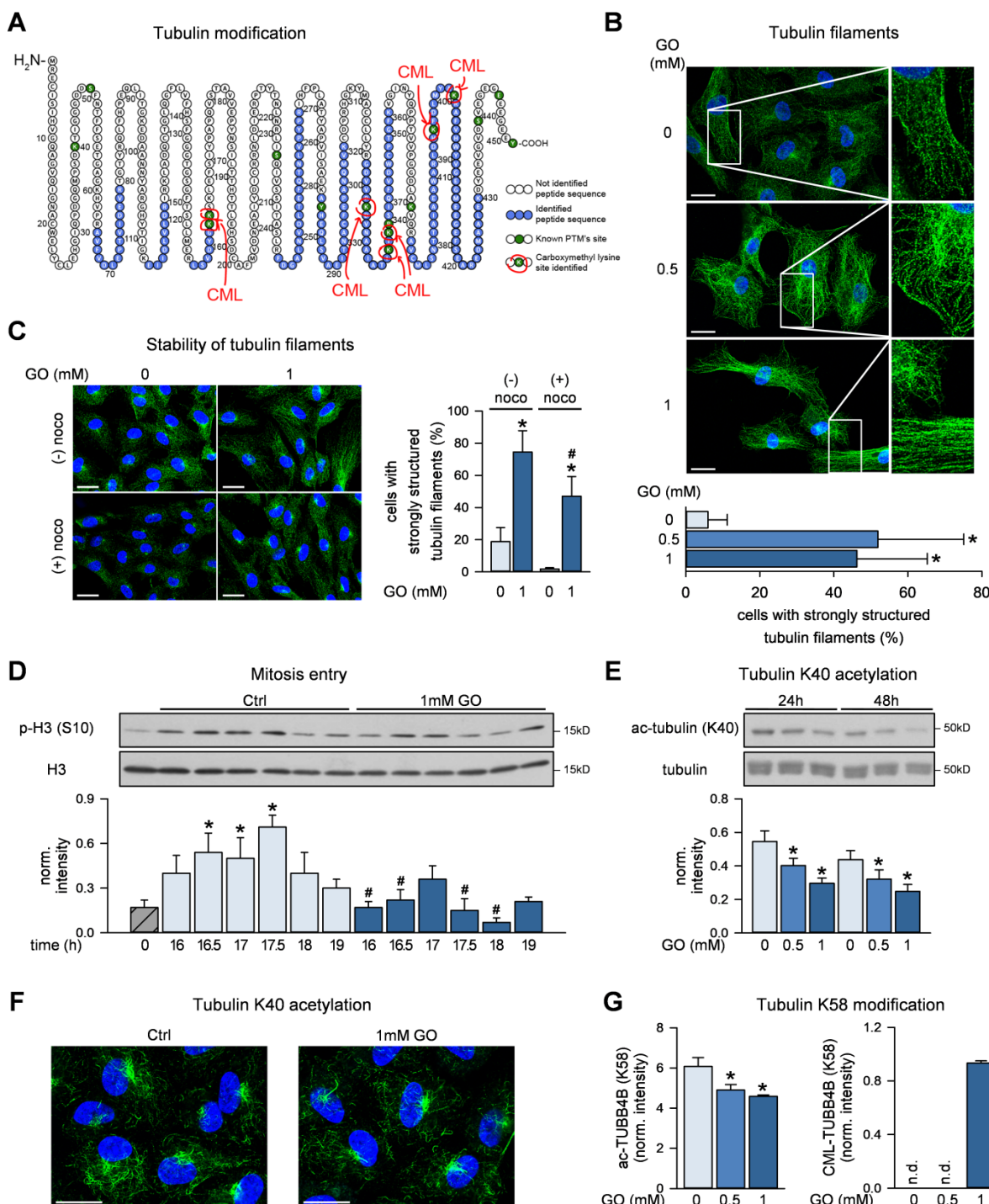
32 regulatory enzymes.

Di Sanzo, Spengler, *et al.*

Figure 6. Glyoxal (GO) affects dynamics and post-translational modification of tubulins.
A. Scheme of detected CML modification sites for tubulin α-1B chain. **B**. HUVEC were treated with GO for 48 h and stained against α/β-tubulin and DAPI. Representative immunofluorescence pictures (upper panel) and the percentage of cells with strongly structured tubulin filaments per high-power field (lower panel) are shown. Scale bar=20 μm. n=4. **C**. HUVEC were treated with GO (1 mM, 48 h). 10 μM nocodazole was added for 2 min and α/β-tubulin and DAPI were stained. Representative pictures (left) and the percentage of cells with strongly structured tubulin filaments per high-power field (right) are shown. Scale bar=20 μm. n=5. **D**. HUVEC were synchronized via a double thymidine block and treated with GO subsequent to releasing the block. Cells were lysed and subjected to immunoblot analysis n=5. **E**. HUVEC were treated with GO, lysed and subjected to immunoblot analysis. n=6. **F**. HUVEC were treated with GO for

16

Di Sanzo, Spengler, *et al.*

1 24 h and stained against ac-tubulin (K40) and DAPI. A representative picture out of n=3 is shown. **G**. HUVEC were
2 treated with GO for 48 h. Tubulin modifications were detected by mass spectrometry after respective enrichment of
3 CML-modified or acetylated lysines. Barplot shows the intensity of tubulin β acetylated (left panel) or CML-modified at
4 K58 (right panel). The peptide used for the barplot is _INVYYNEATGGK*YVPR_. Statistical significance was analyzed
5 using one-way or two-way repeated measurement ANOVA corrected using Holm-Šidák method. * p<0.05 vs. control,
6 # p<0.05 vs. respective non-nocodazole-treated cells (C) or vs. respective non-GO-treated cells (D). Related to Fig.
7 S6.
8

Discussion

10 The impairment of protein homeostasis is a hallmark of aging and age-associated diseases (Hipp

11 et al., 2019; Ori et al., 2015; Santos and Lindner, 2017). While age-related changes in protein

12 abundance and turnover have been described across tissues and in different species, less is

13 known about the extent and potential functional impact of PTM. Here, we focused on CML

14 modification of proteins, a non-enzymatic PTM belonging to the class of AGEs (Delgado-Andrade,

15 2016). We developed an antibody-based method for the enrichment of CML-modified peptides

16 coupled to mass spectrometry for identification and quantification. The mapping of CML sites

17 together with studying the total proteome in cultured cells and aging mouse organs allowed us to

18 link CML modifications to cellular functions and to better understand how these processes may

19 contribute to aging and age-associated metabolic diseases.

20 We validated our method in cultured cells treated with the glycating agent glyoxal and identified

21 over 1000 specific sites of CML modification. CML occurs more often in high abundant proteins

22 that display slower turnover across different cellular compartments. This corresponds to previous

23 studies showing that global AGEs accumulate particularly in tissues characterized by slow protein

24 turnover, such as crystallin lens, cartilage and skin (Gkogkolou and Bohm, 2012; Smuda et al.,

25 2015; Verzijl et al., 2000). Interestingly though, we detected CML-modified peptides across

26 proteins that spanned four orders of magnitude of protein abundance and, conversely, we did not

27 identify CML modifications for all of the most abundant proteins. Keeping in mind potential biases

28 due to limited sensitivity and specific protein sequences not amenable to enzymatic digestion that

29 are inherent to any proteomic analysis, our data suggest the existence of a subset of proteins that

30 are more prone to CML modification than others.

31 We extended our analysis to primary organs collected from young and old mice and showed that

32 our enrichment strategy is able to identify hundreds of physiologically occurring CML sites, some

33 of these previously reported in an independent study in the mouse heart (Ruiz-Meana et al.,

34 2019). The modified proteins were enriched for mitochondrial proteins, histones, cytoskeletal

35 proteins and enzymes involved in detoxification. We additionally developed targeted proteomics

Di Sanzo, Spengler, *et al.*

1   assays that enable the quantification of a subset of CML sites in tissues without prior peptide

2   enrichment. These analyses revealed that the level of CML modification for some sites, i.e.,

3   histone H4-K92 (corresponding to K91 in the mature protein), increased with aging in different

4   organs, while others remained constant. Thus, while global AGE levels increase with age,

5   preferential modification of certain proteins occurs, as previously suggested in plants (Bilova et

6   al., 2017), illustrating the need for targeted investigation of AGE modification sites. Interestingly,

7   increased CML modification in old mice was paralleled by downregulation of the glyoxalase

8   network in all the investigated organs, which may, at least in part, explain the observed increase

9   of CML-modified proteins in old mice. A similar age-associated decline of glyoxalases in rodents

10   and humans has been reported earlier (Kuhla et al., 2006; Sharma-Luthra and Kale, 1994).

11   Our data reveal a substantial overlap between the identified CML sites and other PTM, particularly

12   acetylation and ubiquitination, suggesting that CML modification may interfere with biological

13   processes mediated by these PTM. For instance, K92 on histone H4, which became substantially

14   more modified with CML during aging, has been reported to be also a target of acetylation and

15   glutarylation, which are both involved in the regulation of chromatin structure and dynamics in

16   response to DNA damage (Bao et al., 2019; Ye et al., 2005). Furthermore, global glycation of

17   histone 3 has been shown to compete with acetylation and methylation thereby disrupting

18   chromatin architecture (Zheng et al., 2019; Zheng et al., 2020). Thus, the age-dependent increase

19   in CML modification of histone H4-K92 as seen in our study may contribute to alteration of

20   chromatin and DNA damage responses in old tissues via interfering with other PTM.

21   In order to investigate other potential mechanisms by which AGEs might affect cellular

22   phenotypes, we focused on perturbation of proteostasis. We show that glyoxal specifically affects

23   the proteostasis network in MEF by increasing the abundance of UPS components and eliciting

24   a hormetic effect on proteasome activity. Low doses of glyoxal increased the activity of the

25   proteasome, while high doses did not alter proteasomal activity and led to an accumulation of

26   ubiquitinated proteins. These data are in agreement with earlier reports showing that

27   methylglyoxal is able to upregulate the protein quality control system (Zemva et al., 2017), and to

28   impair the UPS at high levels leading to accumulation of toxic aggregates (Bento et al., 2010). In

29   line with this, low doses of methylglyoxal led to an increased lifespan of *C. elegans*, while high

30   doses (>1 mM) decreased lifespan (Ravichandran et al., 2018). Inhibition of proteasomal activity

31   by dicarbonyls might be related to a direct modification of the 20S proteasome, as previously

32   shown (Queisser et al., 2010). Here, we provide evidence for an interference of high AGEs with

33   the stability of the proteasome by showing reduced thermal stability of proteasomal proteins in

1 glyoxal-treated cells and identifying direct sites of CML modification of proteasomes both in cells

2 treated with glyoxal as well as in organs obtained from mice. Interestingly, we also identified

3 several enzymes involved in the ubiquitin cycle, including ubiquitin itself, to be direct targets of

4 CML modification, suggesting that the interference of AGEs might extend to other components of

5 the UPS beyond the proteasome. Thus, given that the proteasome activity is known to decrease

6 across tissues during aging (Friguet et al., 2000; Hipp et al., 2019; Kelmer Sacramento et al.,

7 2020; Saez and Vilchez, 2014), increased CML levels during aging might contribute to

8 proteostasis impairment via alteration of the UPS.

9 Finally, we investigated the impact of glyoxal on the functional phenotype of endothelial cells,

10 which are well known to be involved in the pathogenesis of age-associated metabolic diseases

11 (Gimbrone and Garcia-Cardena, 2016; Sena et al., 2013). In line with our initial proteomic

12 analysis, we found that glyoxal triggered a proliferation inhibition phenotype characterized by

13 reduced cell proliferation in the presence of serum or bFGF and by lower sprouting in response

14 to VEGF. Glyoxal had only minor effects on endothelial energy metabolism without changes in

15 cellular ATP levels and did not induce cytotoxic effects, as shown by the absence of apoptosis.

16 Our data are in line with previous studies showing that dicarbonyls induce endothelial dysfunction

17 via oxidative stress, inflammatory responses, senescence or apoptosis (Jang et al., 2017; Liu et

18 al., 2012; Navarrete Santos et al., 2017; Sliman et al., 2010; Wang et al., 2019; Yamawaki and

19 Hara, 2008) and that AGEs interfere via RAGE-dependent signaling processes in endothelial cells

20 (Chen et al., 2020; Li et al., 2018; Ravi et al., 2020). Until now, however, the impact of dicarbonyl-

21 induced changes of protein abundance and intracellular protein modifications on endothelial

22 function has not been thoroughly investigated.

23 To unravel mechanisms underlying the glyoxal-induced proliferation inhibition phenotype, we

24 looked at differentially expressed and/or CML-modified proteins related to cell cycle control. We

25 found that various cell cycle regulators were downregulated in glyoxal-treated cells, particularly

26 proteins involved in DNA replication, likely because CDKN1A/p21 was strongly upregulated and

27 thus restricted S phase entry. This pattern was underlined by growth arrest in G0/G1 and G2

28 phases and by activation of a DNA damage response as possible underlying mechanism (Ciccia

29 and Elledge, 2010; Shaltiel et al., 2015). We were able to detect phosphorylation of CHK1 as a

30 marker for an activated G1 and S phase checkpoint and γH2AX foci as indicator of DNA damage,

31 likely DNA double strand breaks (Kuo and Yang, 2008; Zhang and Hunter, 2014). This was

32 paralleled by an upregulation of the p53/p21 pathway, a major DNA damage response effector

33 known to prevent G1/S transition (Abbas and Dutta, 2009; Helton and Chen, 2007). Glyoxal may

34 cause DNA damage by glycation of DNA leading to so-called nucleotide AGEs (Pischetsrieder et

1 al., 1999; Rabbani and Thornalley, 2015; Thornalley, 2008; Waris et al., 2015) or by triggering the

2 formation of ROS (Ahmad et al., 2018). The latter may have contributed to DNA damage in our

3 study, since both mitochondrial and cytosolic ROS levels were enhanced by glyoxal. In addition

4 to the p53/p21 pathway, the enhanced expression of p16, another inhibitor of cyclin-dependent

5 kinases preventing G1/S transition, is likely to contribute to the observed sustained growth arrest

6 (Rayess et al., 2012). Upregulation of p16 may be linked to increased ROS levels induced by

7 glyoxal (Sasaki et al., 2014; Takahashi et al., 2006). Both, p53/p21 and p16 pathways are known

8 to play a role in the induction of premature senescence dependent on the extent and persistence

9 of stress (Campisi and d'Adda di Fagagna, 2007) and may thus also be involved in mediating the

10 moderate senescence response occurring in glyoxal-treated endothelial cells.

11 In addition to changes in protein abundance of cell cycle proteins induced by glyoxal, we observed

12 CML modification of several proteins mainly involved in G2 and M phases of cell cycle. To

13 understand how glycation of specific proteins may add to the glyoxal-induced inhibition of

14 proliferation in endothelial cells, we focused on tubulin, whose α and β chains exhibited several

15 CML modifications. Tubulin chains form protofilaments, which then associate to microtubules. The

16 latter are major constituents of the cytoskeleton and form the mitotic spindle, whose function is to

17 segregate chromosomes during cell division (Goodson and Jonasson, 2018). A major

18 characteristic of tubulin polymers is their dynamic instability, i.e. the rapid transition between

19 growth and shrinkage, which allows rapid reorganization of the cytoskeleton (Brouhard and Rice,

20 2018). Microtubule dynamics is known to be regulated by various PTM such as detyrosination,

21 polyglutamination or acetylation (Song and Brady, 2015). Our data reveal glycation as a

22 previously unknown tubulin modification, which has an impact on microtubule dynamics. We show

23 that glyoxal treatment of endothelial cells triggered the formation of strongly structured tubulin

24 filaments compared to fewer and thinner filaments in control cells, similar as observed with

25 microtubule-stabilizing agents (Berges et al., 2017; Wang et al., 2017). Accordingly, our data

26 reveal an increased stability of CML-modified microtubules. While the depolymerizing compound

27 nocodazole completely dissolved the tubulin filaments in control cells, its effect was significantly

28 reduced in cells pretreated with glyoxal. Microtubule dynamics may not only be affected by CML

29 modification of tubulin but also by competition of glycation with other PTM. As shown in our

30 proteomic analysis of mouse tissues, CML modification often occurs on residues that are known

31 to be modified by other PTM. Accordingly, we found four CML-modified sites on α-tubulin (K326,

32 K336, K394, K401) and three CML sites on β-tubulin (K58, K324, K379), which overlap with

33 previously described acetylation sites (Sadoul and Khochbin, 2016). Moreover, we were able to

34 demonstrate a direct competition between glycation and acetylation for K58 of β-tubulin indicating

1 that exposure of endothelial cells to glyoxal may alter the tubulin code (Ferreira et al., 2018; Janke

2 and Magiera, 2020). The latter refers to the concept that PTM of tubulin modulate the composition

3 of individual microtubules and program them for specific functions, for instance by regulating the

4 interaction with microtubule-binding proteins (Janke and Magiera, 2020). While the functional

5 impact of most acetylation marks is not yet understood, acetylation of K40 within the microtubule

6 lumen is suggested to protect microtubules from mechanical stress, possibly through affecting

7 interaction between tubulin protofilaments (Portran et al., 2017; Xu et al., 2017). We found a

8 decrease in K40 acetylation in glyoxal-treated cells, which adds to the alteration of the tubulin

9 code although CML modification was not detected at this site. To address the question of whether

10 the observed alteration of microtubule dynamics may affect mitosis, we compared mitosis in

11 control and glyoxal-treated cells by employing a model, in which cells were treated with glyoxal

12 after synchronization at the G1/S transition point. We found a lower expression of the mitotic

13 marker p-H3(S10) in the presence of glyoxal indicating inhibition of mitosis which may be

14 attributable to impaired microtubule dynamics and contribute to the antiproliferative effect of

15 glyoxal. Together, these data describe a novel potential mechanism of cell cycle inhibition via

16 posttranslational CML modification of tubulin.

17 The described proliferation inhibition phenotype of endothelial cells induced by glyoxal is likely to

18 be of pathophysiological relevance. It is well known that CML accumulates in tissues in patients

19 with diabetes and/or cardiovascular diseases as well as in aging (Delgado-Andrade, 2016). On

20 the other hand, reduced angiogenesis leading to impaired wound healing is one of the hallmarks

21 of diabetes (Okonkwo and DiPietro, 2017) and also observed in aging (Hodges et al., 2018;

22 Moriya and Minamino, 2017). It is also known that only fully functional endothelial cells are able

23 to generate new blood vessels (Boodhwani and Sellke, 2009; Sun et al., 2009). Thus, the

24 formation of glyoxal and its effect on endothelial cell proliferation may be one of the factors linking

25 metabolic alterations to disturbed angiogenesis in diabetes and aging and promote pathogenetic

26 processes via this mechanism.

27 Together, the data presented in this study are based on a novel enrichment strategy coupled to

28 mass spectrometry, which allowed the identification of proteins susceptible to CML modification

29 and their respective CML sites in cells treated with a glycating agent and in organs from mice.

30 Our data unravel subsets of proteins prone to CML modification as well as a proteotoxic response

31 characterized by a dysfunction of the UPS. Exposure of endothelial cells to glycative stress

32 triggers a proliferation inhibition phenotype, in which altered expression of cell cycle regulators

33 induced via the DNA damage response as well as CML modification of tubulin contribute to growth

34 arrest. The observations of this study expand our understanding of vascular dysfunction in aging

Di Sanzo, Spengler, *et al.*

1   and age-related metabolic disease and pave the way for further studies to link CML modifications

2   to functional phenotypes.

3

Di Sanzo, Spengler, *et al.*

17 **Author contributions:** Conceptualization: SDS, AO, RH. Investigation: SDS, KS, JMK, AL, TLR,

18 TB, CM. Methodology: SDS, KS, JMK. Data analysis: SDS, KS, JMK, LP, TB, AO, AL, TLR, RH.

19 Project administration: AO, RH. Resources: AO, RH, MAG. Supervision: ZQW, MAG, AO, RH.

20 Visualization: SDS, KS, AO. Writing – original draft: SDS, KS, AO, RH. Writing – review & editing:

21 TB, LP and ZQW.

22 **Declaration of interests:** Authors declare no competing interests.

23

23

Di Sanzo, Spengler, *et al.*

1 **Material and Methods**

2

3 *Chemicals*

4 M199 was purchased from Lonza (Verviers, Belgium). Fetal calf serum (FCS), human serum,

5 endothelial growth supplement (ECGS), glyoxal (HUVEC studies), hydroxyurea, nocodazole,

6 antimycin A, thymidine, 2-deoxy-D-glucose, trypsin inhibitor, thrombin, aprotinin, 5-bromo-4-

7 chloro-3-indolyl β-D-galactopyranoside (X-Gal), 4′,6-diamidino-2-phenylindole (DAPI), octyl β-D-

8 glucopyranoside, iodoacetamide (IAA), aqueous NH3, ATP, cOmplete™, EDTA-free protease

9 inhibitor cocktail, HEPES, MOPS, NP40 and PonceauS were purchased from Sigma

10 (Taufkirchen, Germany). Protease inhibitor mixture complete, EDTA-free was obtained from

11 Roche Diagnostics (Mannheim, Germany), fibrinogen from Merck/Millipore (Darmstadt, Germany)

12 and Fluoromount-G® from Southern Biotech (Birmingham, AL, US), respectively. Bovine serum

13 albumin-C (BSA-C) was from Aurion (Wageningen, The Netherlands) and goat serum from Cell

14 Signaling Technology (Frankfurt, Germany). D-glucose, L-glutamine, sodium pyruvate, 5-ethynyl-

15 2′-deoxyuridine, Trypsin-EDTA and anhydrous dimethylsulfoxide (DMSO) derived from Thermo

16 Fisher Scientific (Waltham, MA, USA). Oligomycin and carbonyl cyanide-4-

17 (trifluoromethoxy)phenylhydrazone (FCCP) came from Abcam (Cambridge, UK).

18 Carboxyfluorescein succinimidyl ester (CFSE) was purchased from Invitrogen (Carlsbad, CA,

19 US). Glyoxal (MEF studies), glycerine, β-mercaptoethanol, glucose, dithiothreitol (DTT), EDTA,

20 formic acid, ammonium bicarbonate, Tris, bovine serum albumin, Tween-20 and Triton X-100

21 were obtained from Carl Roth GmbH (Karlsruhe, Germany). Trifluoroacetic acid, acetonitrile and

22 2-propanol were from Biosolve BV (Valkenswaard, The Netherlands) and glycine was from VWR

23 International (Radnor, PA, USA).

24

25 *Antibodies*

26 Antibodies raised against β-actin (HUVEC studies), cleaved caspase 3 (D175), caspase 3,

27 cleaved PARP (D214), PARP, histone 3, p-Chk1 (S317), p-Chk1 (S345), Chk1, γH2A.X (S139),

28 p-p53 (S15), p53, p21, p16, α/β-tubulin and ac-tubulin (K40) were obtained from Cell Signaling

29 Technology (Frankfurt, Germany). Antibodies against CML (western blot) and p-H3 (S10)

30 (western blot) were from Abcam (Cambridge, UK). The antibody against p-H3 (S10) for flow

31 cytometry was obtained from Merck/Millipore (Darmstadt, Germany) and cyclin A antibody was

32 from Santa Cruz Biotechnology (Dallas, TX, US). The CML antibody used for enrichment was

33 purchased from ImmuneChem Pharmaceuticals Inc. (Burnaby, Canada). Antibodies against

34 mono- and K29-, K48-, and K63-linked mono- and polyubiquitinylated proteins were from Enzo

Di Sanzo, Spengler, *et al.*

1   Life Sciences (Farmingdale, NY, USA) and the antibody against β-actin (MEF studies) was from

2   Sigma (Taufkirchen, Germany). Peroxidase-labeled anti-mouse and anti-rabbit IgG were from

3   Kirkegaard and Perry Laboratories, Inc. (Gaithersburg, MD, USA) or from Dako GmbH (Hamburg,

4   Germany). AlexaFluor®647-conjugated azide (AF647 azide) and secondary AlexaFluor®488-

5   conjugated goat anti-rabbit IgG were from Thermo Scientific (Waltham, MA, USA).

6

7   *Mice*

8   All wild-type mice were C57BL/6J obtained from Janvier Labs (Le Genest-Saint-Isle, France) or

9   from internal breeding at FLI. All animals were kept in a specific pathogen-free animal facility with

10 a 12 h light/dark cycle. Young mice were aged 3-4 months, old mice were aged 26-33 months.

11 Mice had unlimited access to food (ssniff, Soest, Germany)) during the experiment. For the

12 analysis of total proteome, CMLpepIP and glyoxalase activity measurements only male mice were

13 used. Mice were euthanized and organs were isolated, washed in PBS, weighted and immediately

14 snap-frozen in liquid nitrogen before storage in -80°C.

15

16 *MEF cell culturing and treatments*

17 SV40-immortalized mouse embryonic fibroblasts (MEF, a kind gift of K. L. Rudolph) were grown

18 in high glucose DMEM medium (Sigma, D6429) until they reached 70 % confluency. For glyoxal

19 treatment, DMEM medium was removed, cells were washed with PBS and live cell imaging

20 medium (140 mM NaCl; 2.5 mM KCl; 1.8 mM $CaCl_2$; 1.0 mM $MgCl_2$), 20 mM HEPES; 4500 mg/l

21 glucose and pH 7.4) was added. Subsequently, glyoxal diluted in the same medium was added

22 at final concentrations of 0.5 or 2 mM for 8 - 24 h, as notified in figures. For all treatments, cells

23 were snap-frozen in liquid nitrogen and stored at -80°C until further processing.

24

25 *HUVEC cell culture and treatment*

26 HUVEC were isolated from anonymously acquired human umbilical cords according to the

27 "Ethical principles for Medical Research Involving Human Subjects" (Declaration of Helsinki 1964)

28 as previously described (Spengler et al., 2020). The protocol was approved by the Jena University

29 Hospital Ethics Committee. The donors were informed and gave written consent. Briefly, after

30 rinsing the cord veins with 0.9 % NaCl, endothelial cells were detached with collagenase (0.01 %,

31 3 min at 37 °C), suspended in M199/10 % FCS, washed once (500 x g, 6 min) and seeded on a

32 cell culture flask coated with 0.2 % gelatin. Full growth medium (M199, 17.5 % FCS, 2.5 % human

33 serum, 7.5 µg/ml ECGS, 7.5 U/ml heparin, 680 µM glutamine, 100 µM vitamin C, 100 U/ml

34 penicillin, 100 µg/ml streptomycin) was added 24 h later. HUVEC from the second passage were

Di Sanzo, Spengler, *et al.*

1 detached with trypsin/EDTA after two washes in PBS and the reaction was stopped with HEPES

2 buffer (10 mM HEPES (pH 7.4), 145 mM NaCl, 5 mM KCl, 1 mM MgSO$_4$, 1.5 mM CaCl$_2$, 10 mM

3 glucose) containing 10 % FCS (HEPES/FCS). Cells were counted using a Neubauer chamber.

4 Seeding was carried out at densities between 23,000/cm² and 27,500/cm² dependent on whether

5 experiments were performed 48 or 72 h after seeding, respectively. For senescence and growth

6 experiments, the seeding density was lower (8,000/cm² (senescence-associated β-galactosidase

7 (SA-β-Gal) staining), 10,000/cm² (BrdU incorporation), 15,000/cm² (cell cycle), 20,500/cm²

8 (thymidine block)). If not otherwise indicated, 30 mm-dishes were used for experiments. For mass

9 spectrometry-based proteomics, detachment of HUVEC from 90 mm-dishes was performed with

10 trypsin/EDTA and the reaction was stopped by an equal amount of trypsin inhibitor (1 mg/ml in

11 PBS). Then, cells were washed twice in M199 (500 x g, 3 min) and snap-frozen in liquid nitrogen.

12 Treatment of HUVEC with glyoxal was performed in experimental medium (i.e. full growth medium

13 without vitamin C) and started 48 - 72 h after seeding. Incubations were performed with glyoxal

14 concentrations of 0.5 or 1 mM for 4 - 48 h, as notified in figures. Thereafter, cells were stimulated

15 with growth factors if indicated and processed as described below.

16

17 *Sample preparation for quantitation of total CML levels*

18 MEF and mouse organs were lysed and proteins acetone precipitated as described in *Sample*

19 *preparation for mass spectrometry-based proteomics.* HUVEC were detached by trypsin/EDTA,

20 transferred to HEPES/FCS, centrifuged (500 x *g*, 6 min), washed twice in 2 ml PBS and subjected

21 to one freezing/thawing cycle in liquid nitrogen. Pellets were resuspended in 200 µl ice-cold Tris

22 buffer (50 mM Tris (pH 7.4), 2 mM EDTA, 1 mM EGTA, 50 mM NaF, 150 mM NaCl, 10 mM

23 Na$_4$P$_2$O$_7$, 1 mM Na$_3$VO$_4$, 1 % Triton X-100, 0.1 % SDS, 0.5 % sodium deoxycholate, 1 mM PMSF,

24 10 µl/ml protease inhibitor cocktail) and incubated on ice for 30 min. After homogenization using

25 a tissue homogenizer, proteins were precipitated by adding TCA to a final concentration of 10 %.

26 Samples were centrifuged (4000 x *g*, 5 min, 4 °C), pellets were washed twice in ice-cold 80 %

27 acetone and stored at -80 °C until further processing.

28

29 *Quantitation of total CML levels by HPLC-MS/MS*

30 Protein pellets were reconstituted in PBS and 250 µl aliquots of protein extracts (1 mg/ml) were

31 reduced by addition of 100 µl NaBH$_4$ solution (15 mg/ml in 0.01 M NaOH) and were shaken for 1

32 h at room temperature. Samples were dried in a vacuum concentrator (Savant-Speed-Vac Plus

33 SC 110 A combined with a Vapor Trap RVT 400, Thermo Fisher Scientific, Bremen, Germany).

34 800 µl of 6 M HCl was added and the solution was heated 20 h at 110°C under an argon

1 atmosphere. Volatiles were removed in a vacuum concentrator and the residue was dissolved in

2 300 µl of ultra-pure water. Samples were filtered through 0.45 µm cellulose acetate Costar SpinX

3 filters (Corning Inc., Corning, USA). After complete hydrolysis, the amount of amino acids in

4 hydrolysates was determined by ninhydrin assay and referenced to a calibration of L-leucine

5 concentrated between 5 and 100 µM as described previously (Smuda et al., 2015). The

6 absorbance was determined at 546 nm with an Infinite M200 microplate reader (Tecan,

7 Männedorf, Switzerland) using 96-well plates.

8 Chromatographic separations were performed on a stainless-steel column (XSelect HSS T3,

9 250×3.0mm, RP18, 5µm, Waters, Milford, USA) using a flow rate of 0.7 ml/min and a column

10 temperature of 25 °C. Eluents were ultra-pure water (A) and a mixture of methanol (Biosolve,

11 0013684102BS) and ultra-pure water (7:3, (v/v); B), both supplemented with 1.2 ml/l

12 heptafluorobutyric acid. Samples were injected (10 µl) at 2% B and run isocratic for 2 min, gradient

13 was changed to 14 % B within 10 min (held for 0 min), 87 % B within 22 min (held for 0 min),

14 100% B within 0.5 min (held for 7 min) and 2 % B within 2.5 min (held 8 min).

15 A PU-2080 Plus quaternary gradient pump with degasser and an AS-2057 Plus autosampler

16 (Jasco, Gross-Umstadt, Germany) were used. The mass analyses were performed using an API

17 4000 quadrupole instrument (Applied Biosystems, Foster City, USA) equipped with an API source

18 using electrospray ionization. The HPLC system was connected directly to the probe of the mass

19 spectrometer. Nitrogen was used as sheath and auxiliary gas. To measure CML the scheduled

20 multiple-reaction monitoring (sMRM) mode of HPLC-MS/MS was used. Quantitation was based

21 on the standard addition method using known amounts of pure CML standard to compensate for

22 matrix effects. The authentic reference compound was added at 0.5, 1, 2, and 4 times the

23 concentration of the analyte in the sample and correlation coefficients were 0.9 or higher.

24

25 *Thermal Proteome Profiling (TPP)*

26 MEF were grown in 150 mm-dishes until they reached 70-80 % confluence. They were treated at

27 different concentration of glyoxal (0, 0.5 mM and 2 mM) for 8 h in imaging medium (as described

28 in "*MEF cells culturing and treatments*"). Cells were harvested using Trypsin-EDTA phenol red

29 (0.05 %) and counted in order to have 10^6 cells per condition in PBS. Thereupon, cell suspensions

30 were split into 10 individual 0.2 ml PCR tubes in equal volumes (100 µl each tube) and quickly

31 span down to reach a final volume of 20 µl of cell suspension in each tube. Tubes were heated

32 at different temperatures for 3 min using a 96 well dry bath ThermoQ (Hangzhou Bioer

33 Technology, Hangzhou, China). Temperatures were: 37, 41, 44, 47, 50, 53, 56, 60, 63 and 67 °C.

34 Cells were then incubated at 25 °C for 3 min, before adding 80 µl of 0.625 % NP40 and being

Di Sanzo, Spengler, *et al.*

1   snap-frozen in liquid nitrogen. Cells were lysed by a thaw-freeze-thaw cycle composed of an

2   incubation step for 5 min at 25 °C, followed by snap freezing, and an additional incubation at 25

3   °C for 5 min. Lysates were transferred to 7 x 20mm polycarbonate thick-wall tubes (Beckman

4   Coulter, Krefeld, Germany) for ultra-centrifugation (centrifuge Optima TLX with rotor TLA 100,

5   Beckman Coulter), which was carried out at 100,000 x g for 20 min at 4 °C. Identical volumes of

6   the resulting supernatants were then taken (32 µl) estimated to correspond to approximately 30

7   µg of protein extract for the 37 °C sample. Samples were reduced with 10 mM DTT for 15 min at

8   45°C and cysteine alkylated with freshly prepared 15 mM IAA for 30min at 25 °C, in the dark.

9   Following reduction and alkylation, proteins were precipitated with ice-cold acetone and digested

10   into peptides, as described in "*Sample preparation for mass spectrometry-based proteomics".*

11

12   *Sample preparation for mass spectrometry-based proteomics*

13   HUVEC and MEF cell pellets (300k and 100k respectively) were thawed, reconstituted in 50 µl of

14   ice-cold PBS and lysed by addition of 50 µl 2 x lysis buffer (2% SDS, 100 mM HEPES pH 8, 20

15   mM DTT). Mouse organs were thawed and transferred into Precellys® lysing kit tubes (Keramik-

16   kit 1.4/2.8 mm, 2 ml (CKM)) containing 1 ml of PBS supplemented with 1 tab of cOmplete™, Mini,

17   EDTA-free Protease Inhibitor per 50 ml. For homogenization, tissues were shaken twice at 6000

18   rpm for 30 s using Precellys® 24 Dual (Bertin Instruments, Montigny-le-Bretonneux, France) and

19   the homogenate was transferred to new 2 ml Eppendorf tubes. Based on estimated protein

20   content (5 % of fresh tissue weight for liver and 8 % for heart and kidney), 100 µg of protein was

21   processed for further analyses. Volumes were adjusted using PBS and one volume equivalent of

22   2x lysis buffer was added.

23   Samples were sonicated in a Bioruptor Plus (Diagenode, Seraing, Belgium) for 10 cycles with 1

24   min ON and 30 s OFF with high intensity at 20 °C. Samples were quickly centrifuged and a second

25   sonication cycle was performed as described above. The lysates were centrifuged at 18,407 x g

26   for 1 min and transferred to new 1.5 ml Eppendorf tubes. Subsequently, samples were reduced

27   using 10 mM DTT for 30 min at room temperature, and alkylated using freshly made 15 mM IAA

28   for 30 min at room temperature in the dark. Subsequently, proteins were acetone precipitated and

29   digested using LysC (Wako sequencing grade) and trypsin (Promega sequencing grade), as

30   described in (Buczak et al., 2020). The digested proteins were then acidified with 10 % (v/v)

31   trifluoracetic acid and desalted using *Waters Oasis® HLB µElution Plate 30 µm* following

32   manufacturer instructions. The eluates were dried down using a vacuum concentrator, and

33   reconstituted samples in 5 % (v/v) acetonitrile, 0.1 % (v/v) formic acid. For Data Independent

34   Acquisition (DIA) based analysis, samples were transferred to an MS vial, diluted to a

1   concentration of 1 µg/µl, and spiked with iRT kit peptides (Biognosys, Zurich, Switzerland) prior

2   to analysis by LC-MS/MS. For Tandem Mass Tags (TMT) based analysis, samples were further

3   processed for TMT labelling as described below.

4

5   *TMT labelling and high pH peptide fractionation for organ aging proteome and TPP*

6   Reconstituted peptides (at 1 µg/µl) were buffered using 100 mM HEPES buffer pH 8.5 (1:1 ratio)

7   for labelling. 10-20 µg peptides were taken for each labelling reaction. TMT-10plex reagents

8   (Thermo Scientific, Waltham, MA, USA) were reconstituted in 41 µl 100 % anhydrous DMSO.

9   TMT labeling was performed by addition of 1.5 µl of the TMT reagent. After 30 min of incubation

10   at room temperature with shaking at 600 rpm in a thermomixer (Eppendorf, Hamburg, Germany),

11   a second portion of TMT reagent (1.5 µl) was added and incubated for another 30 min. After

12   checking labelling efficiency, samples were pooled (45-50 µg total), desalted with *Oasis® HLB*

13   *µElution Plate* and subjected to high pH fractionation prior to MS analysis.

14   Offline high pH reverse phase fractionation was performed using a Waters XBridge C18 column

15   (3.5 µm, 100 x 1.0 mm, Waters) with a Gemini C18, 4 x 2.0 mm SecurityGuard (Phenomenex)

16   cartridge as a guard column on an Agilent 1260 Infinity HPLC, as described in (Buczak et al.,

17   2020). Forty-eight fractions were collected along with the LC separation, which were subsequently

18   pooled into 16 fractions (for liver and kidney) and 24 fractions (heart). Pooled fractions were dried

19   in a vacuum concentrator and then stored at -80°C until LC-MS/MS analysis.

20

21   *LC-MS/MS based on Data Independent Acquisition (DIA) for MEF and HUVEC*

22   Peptides (approx. 1 µg) were separated using a nanoAcquity UPLC M-Class system (Waters

23   Milford, USA) with a trapping (nanoAcquity Symmetry C18, 5 µm, 180 µm x 20 mm) and an

24   analytical column (nanoAcquity BEH C18, 1.7 µm, 75 µm x 250 mm). The outlet of the analytical

25   column was coupled directly to a Q-exactive HF-X (Thermo Fisher, Waltham, MA, USA) using the

26   Proxeon nanospray source. Solvent A was water, 0.1% formic acid and solvent B was acetonitrile,

27   0.1 % formic acid. The samples (approx. 1 µg) were loaded onto the trapping column with a

28   constant flow of solvent A at 5 µl/min. Trapping time was 6 min. Peptides were eluted via the

29   analytical column with a constant flow of 0.3 µl/min. During the elution step, the percentage of

30   solvent B increased in a non-linear fashion from 0 % to 40 % in 90 min. Total runtime was 115

31   min, including clean-up and column re-equilibration. The peptides were introduced into the MS

32   via a Pico-Tip Emitter 360 µm OD x 20 µm ID; 10 µm tip and a spray voltage of 2.2 kV was applied.

33   The capillary temperature was set at 300 °C. The radio frequency (RF) ion funnel was set to 40

34   %.

Di Sanzo, Spengler, *et al.*

1   Data from a subset of conditions were first acquired in data-dependent acquisition (DDA) mode

2   to contribute to a sample specific spectral library. The conditions were as follows: Full scan MS

3   spectra with mass range 350-1650 m/z were acquired in profile mode in the Orbitrap with

4   resolution of 60,000 FWHM. The filling time was set at maximum of 20 ms with limitation of 3 x

5   10^6 ions. The "Top N" method was employed to take the 15 most intense precursor ions (with an

6   intensity threshold of 4 x 10^4) from the full scan MS for fragmentation (using HCD normalized

7   collision energy, 27 %) and quadrupole isolation (1.6 Da window) and measurement in the

8   Orbitrap (resolution 15,000 FWHM, fixed first mass 120 m/z). The peptide match 'preferred' option

9   was selected and the fragmentation was performed after accumulation of 2 x 10^5 ions or after

10   filling time of 25 ms for each precursor ion (whichever occurred first). MS/MS data were acquired

11   in profile mode. Only multiply charged (2+ - 5+) precursor ions were selected for MS/MS. Dynamic

12   exclusion was employed with maximum retention period of 20 s and relative mass window of 10

13   ppm.   Isotopes were excluded. In order to improve the mass accuracy, internal lock mass

14   correction using a background ion (m/z 445.12003) was applied.

15   For DIA, the same gradient conditions were applied to the LC as for the DDA and the MS

16   conditions were varied as described: Full scan MS spectra with mass range 350-1650 m/z were

17   acquired in profile mode in the Orbitrap with resolution of 120,000 FWHM. The default charge

18   state was set to 3+. The filling time was set at maximum of 60 ms with limitation of 3 x 10^6 ions.

19   DIA scans were acquired with 34 mass window segments of differing widths across the MS1 mass

20   range. HCD fragmentation (stepped normalized collision energy; 25.5, 27, 30 %) was applied and

21   MS/MS spectra were acquired with a resolution of 30,000 FWHM with a fixed first mass of 200

22   m/z after accumulation of 3 x 10^6 ions or after filling time of 40 ms (whichever occurred first). Data

23   were acquired in profile mode. For data acquisition and processing of the raw data Xcalibur 4.0

24   and Tune version 2.9 (both Thermo Fisher) were employed.

25

26   *Data processing for DIA*

27   DpD (DDA plus DIA) libraries were then created by searching both the DDA runs and the DIA

28   runs using Spectronaut Pulsar (v10/11, Biognosys, Zurich, Switzerland). The data were searched

29   against species specific protein databases (Uniprot *Mus musculus* or *Homo sapiens*, reviewed

30   entry only, release 2016_01) with a list of common contaminants appended. The data were

31   searched with the following modifications: carbamidomethyl (C) as fixed modification, and

32   oxidation (M), acetyl (protein N-term) and carboxymethyllysine (CML) as variable modifications.

33   A maximum of 3 missed cleavages was allowed. The library search was set to 1 % false discovery

34   rate (FDR) at both protein and peptide levels. This library contained 92,917 precursors,

Di Sanzo, Spengler, *et al.*

1   corresponding to 5,393 protein groups for HUVEC, and 83,207 precursors, corresponding to

2   4,725 protein groups for MEF using Spectronaut protein inference. DIA data were then uploaded

3   and searched against this spectral library using Spectronaut Professional (v.11) and default

4   settings. Relative quantification was performed in Spectronaut for each pairwise comparison

5   using the replicate samples from each condition using default settings, except: Major Group

6   Quantity = Sum peptide quantity; Major Group Top N = OFF; Minor Group Quantity = Sum

7   precursor quantity; Minor Group Top N = OFF; Data Filtering = Q value sparse; Normalization

8   Strategy = Local normalization; Row Selection = Q value complete. The data (candidate tables)

9   and protein quantity data reports were then exported and further data analyses and visualization

10   were performed with R (v.3.6.3) and R studio server (v. 1.2.5042) using in-house pipelines and

11   scripts.

12

13   *LC-MS/MS based on Tandem Mass Tags (TMT) for organ aging proteome and TPP*

14   For TMT experiments, fractions were resuspended in 10 µl reconstitution buffer (5% (v/v)

15   acetonitrile, 0.1 % (v/v) trifluoroacetic acid in water) and 3 µl were injected. Peptides were

16   analyzed as described in (Buczak et al., 2020) using a nanoAcquity UPLC system (Waters) fitted

17   with a trapping (nanoAcquity Symmetry C18, 5 µm, 180 µm x 20 mm) and an analytical column

18   (nanoAcquity BEH C18, 2.5 µm, 75 µm x 250 mm), and coupled to an Orbitrap Fusion Lumos

19   (Thermo Fisher Scientific, Waltham, MA, USA). Briefly, peptides were separated using a 130 min

20   nonlinear gradient. Full scan MS spectra with mass range 375-1500 m/z were acquired in profile

21   mode in the Orbitrap with resolution of 60,000 FWHM using the quad isolation. The RF on the ion

22   funnel was set to 40 %. The filling time was set at maximum of 100 ms with an AGC target of 4 x

23   10^5 ions and 1 microscan. The peptide monoisotopic precursor selection was enabled along with

24   relaxed restrictions if too few precursors were found. The most intense ions (instrument operated

25   for a 3 s cycle time) from the full scan MS were selected for MS2, using quadrupole isolation and

26   a window of 1Da. HCD was performed with collision energy of 35 %. A maximum fill time of 50

27   ms for each precursor ion was set. MS2 data were acquired with fixed first mass of 120 m/z. The

28   dynamic exclusion list was with a maximum retention period of 60 sec and relative mass window

29   of 10 ppm. The instrument was not set to inject ions for all available parallelizable time. For the

30   MS3, the precursor selection window was set to the range 400-2000 m/z, with an exclude width

31   of 18 m/z (high) and 5 m/z (low). The most intense fragments from the MS2 experiment were co-

32   isolated (using Synchronus Precursor Selection=8) and fragmented using HCD (65 %). MS3

33   spectra were acquired in the Orbitrap over the mass range 100-1000 m/z and resolution set to

Di Sanzo, Spengler, *et al.*

1   30000. The maximum injection time was set to 105 ms and the instrument was set not to inject

2   ions for all available parallelizable time.

3

4   *Data processing for TMT*

5   TMT-10plex data from aging mouse organs were processed using Proteome Discoverer v2.0

6   (Thermo Fisher Scientific, Waltham, MA, USA). Data were searched against the fasta database

7   (Uniprot *Mus musculus* database, reviewed entry only, release 2016_01) using Mascot v2.5.1

8   (Matrix Science) with the following settings: Enzyme was set to trypsin, with up to 1 missed

9   cleavage. MS1 mass tolerance was set to 10ppm and MS2 to 0.5Da. Carbamidomethyl cysteine

10 was set as a fixed modification and oxidation of methionine as variable. Other modifications

11 included the TMT-10plex modification from the quantification method used. The quantification

12 method was set for reporter ions quantification with HCD and MS3 (mass tolerance, 20 ppm).

13 The false discovery rate for peptide-spectrum matches (PSMs) was set to 0.01 using Percolator

14 (Brosch et al., 2009).

15 Reporter ion intensity values for the PSMs were exported and processed with procedures written

16 in R (v.3.6.3) and R studio server (v. 1.2.5042), as described in (Heinze et al., 2018). Briefly,

17 PSMs mapping to reverse or contaminant hits, or having a Mascot score below 15, or having

18 reporter ion intensities below 1×10^3 in all the relevant TMT channels were discarded. TMT

19 channels intensities from the retained PSMs were then log_2 transformed, normalized and

20 summarized into protein group quantities by taking the median value using MSnbase (Gatto and

21 Lilley, 2012). At least two unique peptides per protein were required for the identification and only

22 those peptides with no missing values across all 10 channels were considered for quantification.

23 Protein differential expression was evaluated using the limma package (Ritchie et al., 2015).

24 Differences in protein abundances were statistically determined using the Student's t test

25 moderated by the empirical Bayes method. P values were adjusted for multiple testing using the

26 Benjamini-Hochberg method (FDR, denoted as "adj. p") (Benjamini and Hochberg, 1995).

27

28 *Data processing for TPP*

29 For the analysis of the TPP sample data (TMT10plex, high pH fractionated, MS3 data acquisition),

30 raw data files were first processed through the preMascot process of the isobarquant package

31 (Franken et al., 2015). After the .mgf files had been generated, these were processed via Mascot

32 Daemon (Matrix Science) using Mascot version 2.5.1. Firstly, species-specific database including

33 decoy was created by concatenating the forward entries (Uniprot *Mus musculus* database,

34 reviewed entry only, release 2016_01) to the reversed sequences of the database. Data were

1 then searched against the relevant database with the following settings: Enzyme = trypsin, 3

2 missed cleavage allowed.   Modifications: carbamidomethyl (C) and TMT10plex (K) as fixed

3 modifications; oxidation (M), carboxymethyllysine (K) and TMT10plex (N-term) as variable. MS1

4 tolerance was 10 ppm, MS2; 0.5 Da. When the .dat files for each fraction had been generated,

5 these were subjected to the postMascot process of isobarquant, combining all the outputs into a

6 single, merged, TMT10plex quantified protein output for further processing of melting point curves

7 using the TPP package in R (Childs et al., 2019).

8

9 *Enrichment of CML modified peptides (CMLpepIP)*

10 Lysates containing approximatively 1 mg protein for HUVEC and MEF and 5 mg for tissues were

11 digested as described in "*Sample preparation for mass spectrometry-based proteomics*" with

12 minor modifications: the digestion buffer used was 3 M Urea, 100 mM HEPES, 5 % (v/v) acetonitrile

13 and the ratio of LysC and Trypsin used was 1:150 enzyme to protein. The digests were then

14 acidified with 10 % (v/v) trifluoroacetic acid and then desalted with *Waters Oasis® HLB 96-well Plate*

15 *30 µm* (Waters Corp., Milford, MA, USA) in the presence of a slow vacuum. In this process, the

16 columns were conditioned with 2x 1000 µl solvent B (80% (v/v) acetonitrile; 0.05 % (v/v) formic

17 acid) and equilibrated with 2x 1000 µl solvent A (0.05% (v/v) formic acid in milliQ water). The

18 samples were loaded, washed 2 times with 1000 µl solvent A, and then eluted with 500 µl solvent

19 B. The eluates were dried down and dissolved in 200 µl of IP buffer (50 mM MOPS, pH 7.3, 10

20 mM KPO_4 pH 7.5, 50 mM HEPES, 2.5 mM octyl β-D-glucopyranoside) at concentration of 5 µg/µl

21 followed by sonication in a Bioruptor Plus (5 cycles with 1 min ON and 30 s OFF with high intensity

22 at 20 °C). 10 % of the sample was kept and analyzed separately as input control. A pre-cleaning

23 step was applied by incubating each sample with 10 µl of Protein A magnetic beads (New England

24 Biolabs GmbH, Frankfurt, Germany) for 1 h at 4 °C in tube roller (15 rpm) (STARLAB Tube roller

25 Mixer RM Multi-1). Samples were transferred to a magnetic rack (DynaMag™-2, Invitrogen). The

26 supernatant was transferred into a new 1.5 ml Eppendorf tube and incubated overnight with 30

27 µg of pan (ε-N) CML antibody at 4 °C on tube roller (15 rpm) (STARLAB Tube roller Mixer RM

28 Multi-1). Subsequently, 150 µl of Protein A magnetic beads were added to the samples and

29 incubated for 1 h at 4°C on tube roller as previously. Samples were then transferred to a magnetic

30 rack and the flow through was collected in a fresh tube, and beads were washed 3 times in 300

31 µl IP buffer. The enriched peptides were then eluted 3 times in 54 µl of 0.1 M glycine pH 2.6. The

32 fraction of elution, flow through and the input were desalted using Macro Spin Column C18

33 columns (Harvard Apparatus, Cambridge, MA, USA) following manufacturer instructions. The

34 eluates were then dried down in a vacuum concentrator, dissolved in in 5 % (v/v) acetonitrile, 0.1

1 % (v/v) formic acid and directly analyzed by LC-MS/MS for the MEF and HUVEC. An additional

2 step of high pH peptide fractionation was performed for eluates from mouse organs, as described

3 in "*TMT labelling and high pH peptide fractionation for organ aging proteome and TPP".* Eight

4 pooled fractions from high pH fractionation were measured by LC-MS/MS for each sample.

5

6 *LC-MS/MS based on Data Dependent Acquisition (DDA) for CMLpepIP*

7 Peptides were separated using the nanoAcquity UPLC system (Waters) fitted with a trapping

8 (nanoAcquity Symmetry C18, 5 µm, 180 µm x 20 mm) and an analytical column (nanoAcquity

9 BEH C18, 1.7 µm, 75 µm x 250 mm). The outlet of the analytical column was coupled directly to

10 an Orbitrap Fusion Lumos (Thermo Fisher Scientific, Waltham, MA, USA) using the Proxeon

11 nanospray source. Solvent A was water, 0.1 % (v/v) formic acid and solvent B was acetonitrile,

12 0.1 % (v/v) formic acid. The samples (500 ng) were loaded with a constant flow of solvent A at

13 5 µl/min onto the trapping column. Trapping time was 6 min. Peptides were eluted via the

14 analytical column with a constant flow of 0.3 µl/min. During the elution step, the percentage of

15 solvent B increased in a linear fashion from 3 % to 25 % in 30 min, then increased to 32 % in 5

16 more minutes and finally to 50 % in a further 0.1 min. Total runtime was 60 min. The peptides

17 were introduced into the mass spectrometer via a Pico-Tip Emitter 360 µm OD x 20 µm ID; 10

18 µm tip (New Objective) and a spray voltage of 2.2 kV was applied. The capillary temperature was

19 set at 300 °C. The RF lens was set to 30 %. Full scan MS spectra with mass range 375-1500 m/z

20 were acquired in profile mode in the Orbitrap with resolution of 120,000 FWHM. The filling time

21 was set at maximum of 50 ms with limitation of 2×10^5 ions. The "Top Speed" method was

22 employed to take the maximum number of precursor ions (with an intensity threshold of 5×10^3)

23 from the full scan MS for fragmentation (using HCD collision energy, 30 %) and quadrupole

24 isolation (1.4 Da window) and measurement in the ion trap, with a cycle time of 3 s. The MIPS

25 (monoisotopic precursor selection) peptide algorithm was employed but with relaxed restrictions

26 when too few precursors meeting the criteria were found. The fragmentation was performed after

27 accumulation of 2×10^3 ions or after filling time of 300 ms for each precursor ion (whichever

28 occurred first). MS/MS data were acquired in centroid mode, with the rapid scan rate and a fixed

29 first mass of 120 m/z. Only multiply charged (2+ - 7+) precursor ions were selected for MS/MS.

30 Dynamic exclusion was employed with maximum retention period of 60 s and relative mass

31 window of 10 ppm. Isotopes were excluded. Additionally, only 1 data dependent scan was

32 performed per precursor (only the most intense charge state selected). Ions were injected for all

33 available parallelizable time. In order to improve the mass accuracy, a lock mass correction using

Di Sanzo, Spengler, *et al.*

1   a background ion (m/z 445.12003) was applied. For data acquisition and processing of the raw

2   data, Xcalibur 4.0 (Thermo Scientific, Waltham, MS, USA) and Tune version 2.1 were employed.

3

4   *Data processing for DDA for CMLpepIP*

5   Software MaxQuant (version 1.5.3.28) was used to search the data. The data were searched

6   against species-specific databases (Uniprot *Mus musculus* or *Homo sapiens*, reviewed entry only,

7   release 2016_01) with a list of common contaminants appended. The data were searched with

8   the following modifications: carbamidomethyl (C) as fixed modification, and oxidation (M), acetyl

9   (protein N-term) and carboxymethyllysine (CML) as variable modifications. The mass error

10   tolerance for the full scan MS spectra was set at 20 ppm and for the MS/MS spectra at 0.5 Da. A

11   maximum of 3 missed cleavages were allowed. Peptide and protein level 1 % FDR were applied

12   using a target-decoy strategy (Elias and Gygi, 2007). MaxQuant outputs were then used to

13   perform qualitative analyses. In addition, highly confident CML sites were defined using these

14   additional parameters: Posterior Error Probability <0.05, score >50, score difference >5,

15   localization probability >0.75.

16

17   *Enrichment of acetylated peptides*

18   HUVEC pellets (3 biological replicates per condition/time point) corresponding to approximately

19   500µg of proteins were used. Cell pellets were thawed, lysed and digested as described in the

20   paragraph "*Sample preparation for mass spectrometry-based proteomics"*. The digested peptides

21   were acidified with 10% (v/v) trifluoroacetic acid and then desalted with *Waters Oasis® HLB 96-*

22   *well Plate 30 µm* following manufacturer instructions. The eluates were dried down and dissolved

23   in 500 µl of IP buffer (50 mM MOPS pH 7.3, 10 mM KPO4 pH 7.5, 50 mM NaCl, 2.5 mM Octyl β-

24   D-glucopyranoside) to reach a peptide concentration of 1 µg/µl, followed by sonication in a

25   Bioruptor (5 cycles with 1 min ON and 30 s OFF with high intensity at 20°C). 10 % of the sample

26   was kept as it is in order to use it as input. Agarose beads coupled to antibody against acetyl

27   lysine were washed three times with washing buffer (20 mM MOPS pH 7.4, 10 mM KPO$_4$ pH 7.5,

28   50 mM NaCl) before incubation with each sample-peptide for 1.5 h on a rotating well at 750 rpm

29   (STARLAB Tube roller Mixer RM Multi-1). Samples were transferred into Clearspin filter

30   microtubes (0.22 µm) (Dominique Dutscher SAS, Brumath, France) and centrifuged at 4 °C for 1

31   min at 2,000 x *g*. Beads were washed first with IP buffer (three times), then with washing buffer

32   (three times) and finally with 5 mM ammonium bicarbonate (three times). Thereupon, the enriched

33   peptides were then eluted first in basic condition using 50 mM aqueous NH$_3$, then using 0.1 %

34   (v/v) trifluoroacetic acid in 10% (v/v) 2-propanol and finally with 0.1 % (v/v) trifluoroacetic acid.

Di Sanzo, Spengler, *et al.*

1   Elutions were then dried down and reconstituted in MS buffer A (5 % (v/v) acetonitrile, 0.1 % (v/v)

2   formic acid), acidified with 10 % (v/v) trifluoroacetic acid and then desalted with *Waters Oasis®*

3   *HLB µElution Plate 30 µm*. Desalted peptides were finally dissolved in MS buffer A and analyze

4   by LC-MS/MS.

5

6   *LC-MS/MS based on Data Independent Acquisition (DIA) for acetylated peptides*

7   Peptides were separated using the nanoAcquity UPLC system (Waters) fitted with a trapping

8   (nanoAcquity Symmetry C18, 5 µm, 180 µm x 20 mm) and an analytical column (nanoAcquity

9   BEH C18, 1.7 µm, 75 µm x 250 mm). The outlet of the analytical column was coupled directly to

10   an Orbitrap Fusion Lumos (Thermo Fisher Scientific, Waltham, MA. USA) using the Proxeon

11   nanospray source. Solvent A was water, 0.1 % (v/v) formic acid and solvent B was acetonitrile,

12   0.1 % (v/v) formic acid. The samples (approx. 1 µg for DDA and 3 µg for DIA) were loaded with a

13   constant flow of solvent A at 5 µl/min onto the trapping column. Trapping time was 6 min.

14   Peptides were eluted via the analytical column with a constant flow of 0.3 µl/min. During the elution

15   step, the percentage of solvent B increased in a non-linear fashion from 0 % to 40 % in 40 min.

16   Total runtime was 60 min, including clean-up and column re-equilibration. The peptides were

17   introduced into the mass spectrometer via a Pico-Tip Emitter 360 µm OD x 20 µm ID; 10 µm tip

18   (New Objective) and a spray voltage of 2.2 kV was applied. The capillary temperature was set at

19   300 °C. The RF lens was set to 30 %. Data from each sample were first acquired in DDA mode.

20   The conditions were as follows: Full scan MS spectra with mass range 350-1650 m/z were

21   acquired in profile mode in the Orbitrap with resolution of 60,000 FWHM. The filling time was set

22   at maximum of 50 ms with limitation of 2×10^5 ions. The "Top Speed" method was employed to

23   take the maximum number of precursor ions (with an intensity threshold of 5×10^4) from the full

24   scan MS for fragmentation (using HCD collision energy, 30 %) and quadrupole isolation (1.4 Da

25   window) and measurement in the Orbitrap (resolution 15,000 FWHM, fixed first mass 120 m/z),

26   with a cycle time of 3 s. The MIPS (monoisotopic precursor selection) peptide algorithm was

27   employed but with relaxed restrictions when too few precursors meeting the criteria were found.

28   The fragmentation was performed after accumulation of 2×10^5 ions or after filling time of 22 ms

29   for each precursor ion (whichever occurred first). MS/MS data were acquired in centroid mode.

30   Only multiply charged (2^+ - 7^+) precursor ions were selected for MS/MS. Dynamic exclusion was

31   employed with maximum retention period of 15 s and relative mass window of 10 ppm. Isotopes

32   were excluded. In order to improve the mass accuracy, internal lock mass correction using a

33   background ion (m/z 445.12003) was applied. For data acquisition and processing of the raw data

34   Xcalibur 4.0 (Thermo Scientific, Waltham, MA, USA)) and Tune version 2.1 were employed.

Di Sanzo, Spengler, *et al.*

1   For the DIA data acquisition the same gradient conditions were applied to the LC as for the DDA

2   and the MS conditions were varied as described: Full scan MS spectra with mass range 350-

3   1650m/z were acquired in profile mode in the Orbitrap with resolution of 120,000 FWHM. The

4   filling time was set at maximum of 20 ms with limitation of 5×10^5 ions. DIA scans were acquired

5   with 30 mass window segments of differing widths across the MS1 mass range with a cycle time

6   of 3 s. HCD fragmentation (30 % collision energy) was applied and MS/MS spectra were acquired

7   in the Orbitrap with a resolution of 30,000 FWHM over the mass range 200-2000 m/z after

8   accumulation of 2×10^5 ions or after filling time of 70 ms (whichever occurred first). Ions were

9   injected for all available parallelizable time). Data were acquired in profile mode.

10

11   *Data processing for DIA for acetylated peptides*

12   DpD (DDA plus DIA) libraries were created by searching both DDA and DIA runs using

13   Spectronaut Pulsar (v.13), as described in "*Data processing for DIA*" with the following

14   modification: acetyl (K) was included as variable modification. The library contained 17,051

15   precursors, corresponding to 3,227 protein groups using Spectronaut protein inference. DIA data

16   were then uploaded and searched against this spectral library using Spectronaut Professional

17   (v.13) and default settings. Intensities of precursors deriving from acetylated peptide were

18   obtained from the peptide report table and filtered for a localization score >= 0.75 and further

19   processed using in house written scripts in R (v.3.6.3) and R studio server (v. 1.2.5042).

20   Intensities were summarized at the level of acetylation site by summing the intensities of all the

21   precursors containing a given acetylation sites. Acetylation site intensities were normalized across

22   runs by $\log_2$ transformation and median centering.

23

24   *Parallel Reaction Monitoring (PRM) for CML modified peptides*

25   Twenty-four peptides containing CML-modification were selected among the most confident and

26   consistently identified peptides from CMLpepIP and their isotopically labelled version (heavy

27   Arginine (U-13C6;U-15N4) or Lysine (U-13C6; U-15N2) at the C-term was added) synthesized by

28   JPT Peptide Technologies GmbH (Berlin, Germany). Peptides were delivered as lyophilized and

29   reconstituted in 20 % (v/v) acetonitrile, 0.1 % (v/v) formic acid and further pooled together in a

30   ratio 1:1. An aliquot of the pooled peptides, corresponding to approximatively 150 fmol per

31   peptide, was analyzed by both DDA and DIA LC-MS/MS and used for assay generation using

32   Spectrodive v.9 (Biognosys AG, Schlieren, Switzerland). Assays were successfully developed for

33   20 out of 22 targeted peptides.

Di Sanzo, Spengler, *et al.*

1   Following assay development, the heavy synthetic peptide pool was used to evaluate the limit of

2   detection (LOD) and limit of blank (LOB). Synthetic peptide pool was mixed with 200 ng/µl of

3   digested yeast peptides at concentration from 45 fmol to 5760 fmol on column and measured in

4   triplicate using PRM. Peptides were separated using a nanoAcquity UPLC M-Class system

5   (Waters, Milfors, MA, USA)) with a trapping (nanoAcquity Symmetry C18, 5 µm, 180 µm x 20 mm)

6   and an analytical column (nanoAcquity BEH C18, 1.7 µm, 75 µm x 250 mm). The outlet of the

7   analytical column was coupled directly to a Q-exactive HF-X (Thermo Fisher, Waltham, MA,

8   Germany) using the Proxeon nanospray source. Solvent A was water, 0.1 % (v/v) formic acid and

9   solvent B was acetonitrile, 0.1 % (v/v) formic acid. Peptides were eluted via the analytical column

10   with a constant flow of 0.3 µl/min. During the elution step, the percentage of solvent B increased

11   in a non-linear fashion from 0 % to 40 % in 40 min. Total runtime was 60 min, including clean-up

12   and column re-equilibration. PRM acquisition was performed in a scheduled fashion for the

13   duration of the entire gradient (after instrument calibration in an unscheduled mode) using the

14   "DIA" mode with the following settings: resolution 120,000 FWHM, AGC target 3×10^6, maximum

15   injection time (IT) 250 ms, isolation window 0.4 m/z. For each cycle, a "full MS" scan was acquired

16   with the following settings: resolution 120,000 FWHM, AGC target 3×10^6, maximum injection

17   time (IT) 10 ms, scan range 350 to 1650 m/z. Peak group identification and quantification was

18   performed using SpectroDive v9. Quantification was performed using spike-in approach. Thereby,

19   the summed height of all the identified transitions was used to estimate the quantity of each

20   peptide. LOQ and LOB was performed using the R package MSstat (Choi et al., 2014) using non-

21   linear mode.

22   For CML site quantification in aging organs, not enriched digested peptides were spiked with

23   synthetic heavy peptides at a concentration of 144 fmol/µl and analyzed by scheduled PRM as

24   described above, using the following sub-panel:

25

Protein Access	GeneID	Peptide sequence	Charge state
P41216	Acsl1	IFGQANTSLK[CML]R	+2, +3
P48036	Anxa5	DLVDDLK[CML]SELTGK	+2
Q03265	Atp5a1	VVDALGNAIDGK[CML]GPIGSK	+2, +3
P56480	Atp5b	GVQK[CML]ILQDYK	+2
Q91VR2	Atp5c1	THSDQFLVSFK[CML]DVGR	+3
Q9CQQ7	Atp5f1	QIQDAIDMEK[CML]AQQALVQK	+2
Q9DB20	Atp5o	VSLAVLNPYIK[CML]R	+3
P24270	Cat	DAQLFIQK[CML]K	+2
Q8BH95	Echs1	AFAAGADIK[CML]EMQNR	+3

Di Sanzo, Spengler, *et al.*

Q9DBM2	Ehhadh	FAQTVIGK[CML]PIEPR	+2, +3
Q8BMS1	Hadha	FVDLYGAQK[CML]VVDR	+3
P01942	Hba	FLASVSTVLTSK[CML]YR	+3
P62806	Hist1h4a	TVTAMDVVYALK[CML]R	+3
Q7TMF3	Ndufa12	MELVEVLK[CML]R	+2
P48962	Slc25a4	IAK[CML]DEGANAFFK	+3
Q78IK2	Usmg5	AGAESDGQFQFTGIK[CML]K	+2

1

2 Peptides quantities were normalized across samples by dividing for the integrated intensity of the

3 Base Peak Chromatogram extracted for each sample from "full MS" scans using Xcalibur v4.1.

4

5 *Immunoblot for mono and polyubiquitinated proteins of MEF cells treated with glyoxal*

6 The same cell lysates used for proteasome activity assay were used. Lysates were thawed and

7 centrifugated at 20817 x *g*, for 15 min at 4 °C to remove debris and the supernatant was

8 transferred to a new tube. Based on EZQ assay performed on it, 20 μg of proteins were used.

9 Samples were sonicated for 10 cycles (1min ON and 30s OFF) using a Bioruptor Plus with 4x

10 loading buffer (1.5 M Tris .pH 6.8, 20% (w/v) SDS, 85 % (v/v) glycerin, 5 % (v/v) β-

11 mercaptoethanol). Proteins were separated on 4–20 % Mini-Protean® TGX™ Gels (BioRad,

12 Neuberg, Germany) by sodium dodecyl sulfate polyacrylamide gel electrophoresis (SDS-PAGE)

13 using a Mini-Protean® Tetra Cell system (BioRad, Neuberg, Germany). Proteins were transferred

14 to a nitrocellulose membrane (Millipore) using a Trans-Blot® Turbo™ Transfer Starter System.

15 Membranes were stained with PonceauS for 5 min on a shaker (Heidolph Duomax 1030), washed

16 with milliQ water, imaged on a Molecular Imager ChemiDocTM XRS+ Imaging system (BioRad,

17 Neuberg, Germany) and destained by 2 washes with PBS and 2 washes in TBST for 5 min (Tris-

18 buffered saline (TBS, 25 mM Tris, 75 mM NaCl), with 0.5 % (v/v) Tween-20). After incubation for

19 1 h in blocking buffer (3 % bovine serum albumin (w/v) in TBST), membranes were stained

20 overnight with primary antibodies against mono- and K29-, K48-, and K63-linked mono- and

21 polyubiquitinylated proteins or β-actin diluted in blocking buffer (1:5000) at 4 °C on a tube roller

22 (BioCote® Stuart® SRT6). Membranes were washed 3 times with TBST for 10 min at room

23 temperature (RT) and incubated with horse radish peroxidase coupled secondary antibodies at

24 RT for 1 h (1:2000 in 0.3 % (w/v) BSA in TBST). After 3 more washes for 10 min in TBST,

25 chemiluminescent signals were detected using an ECL (enhanced chemiluminescence) detection

26 kit (Thermo Fisher Scientific, Waltham, MA, USA). Signals were acquired on the Molecular Imager

27 ChemiDocTM XRS+ Imaging system (BioRad, Neuberg, Germany) and analyzed using the Fiji

28 application (Schindelin et al., 2012). Membranes were stripped using stripping buffer (1 % (w/v)

Di Sanzo, Spengler, *et al.*

1 SDS, 0.2 M glycine, pH 2.5), washed 3 times with TBST, blocked and incubated with the second

2 primary antibody, if necessary.

3

4 *Proteasome activity assay on MEF cells treated with glyoxal*

5 Proteasome activity assay was performed using the 20S proteasome activity assay kit (Millipore,

6 Billerica, MA, USA) following the manufacturer instructions. Briefly, cell pellets were thawed and

7 ice-cold lysis buffer (50 mM HEPES pH 7.5, 5 mM EDTA, 150 mM NaCl, 1 % (v/v) Triton X-100,

8 2 mM ATP) was added and left on ice for 30 min with quick vortex steps any 10 min. Samples

9 were centrifuged at 20817 x *g*, for 15 min at 4°C to remove any debris. For protein estimation, a

10 small aliquot was used in order to perform EZQ® Protein Quantitation Kit (Thermo Scientific,

11 Waltham, MA, USA). 50 µg of protein extract were incubated with fluorophore-linked peptide

12 substrate (LLVY-7-amino-4-methylcoumarin [AMC], from the same kit) for 60 min at 37°C.

13 Proteasome activity was measured by quantification of fluorescent units from cleaved AMC at

14 380/460 nm using a microplate reader m1000 (Tecan). Samples were measured together with

15 positive control supplied with the kit.

16

17 *Glyoxalase 1 activity assay*

18 Glyoxalase 1 activity was measured using the ab241019 Glyoxalase I Assay Kit (Colorimetric,

19 Abcam, Cambridge, UK) following manufacturer instructions. Briefly, equal volumes of tissue

20 homogenates (obtained as described above) from heart, liver and kidney, corresponding to an

21 estimated protein amount of 50 µg were analyzed. The substrate mix was prepared and left for 10

22 min at RT in the darkness to allow the formation of hemimercaptal. Afterwards, samples were

23 transferred to a 96 well-plate and the substrate mix was added. The formation of S-D-

24 lactoylglutathione (SLG) was monitored for 30 min in a kinetic mode by using a microplate reader

25 m1000 (Tecan) at OD 240 nm. The activity was then calculated using the formula suggested by

26 the vendors and normalized for equal loading using immunoblot against beta-actin (as described

27 in "*Immunoblot for mono and polyubiquitinated proteins of MEF cells treated with glyoxal*")

28 performed on the same homogenates.

29

30 *Other data analyses*

31 Gene Ontology enrichment based on ClueGO v2.5.6 (Bindea et al., 2009) was performed using

32 the table S2 (highly confident sites) as input, and by applying the following parameters: for heart

33 (Kappa score threshold 0.4, minimum percentage =5 and number of genes =3), for kidney (Kappa

34 score threshold 0.4, minimum percentage =2 and number of genes =3) and for liver (Kappa score

Di Sanzo, Spengler, *et al.*

1　threshold 0.4, minimum percentage =2 and number of genes =3). Statistical test used =

2　Enrichment/depletion (Two-side hypergeometric test). For the overlap between HUVEC cells and

3　MEF cells, the following parameters were applied: Kappa score threshold 0.4, minimum

4　percentage =4 and number of gene =2). Statistical test used = Enrichment/depletion (Two-side

5　hypergeometric test).

6　KEGG pathway and Gene Ontology enrichments for MEF and HUVEC total proteome were

7　performed by Gene Set Enrichment Analysis (GSEA) with WebGestalt (Liao et al., 2019) using

8　the entire lists of quantified proteins ranked on the basis of the measured log2 fold changes.

9

10　*HUVEC lysis and western blot*

11　HUVEC were lysed in ice-cold Tris buffer (50 mM Tris (pH 7.4), 2 mM EDTA, 1 mM EGTA, 50

12　mM NaF, 10 mM $Na_4P_2O_7$, 1 mM Na_3VO_4, 1 mM DTT, 1 % Triton X-100, 0.1 % SDS, 1 mM PMSF,

13　10 µl/ml protease inhibitor cocktail) for 15 min on ice, scraped and centrifuged (700 x g, 6 min).

14　Aliquots of supernatants were used for protein determination according to Lowry. Lysates were

15　supplemented with Laemmli buffer, subjected to SDS-PAGE (25-50 µg lysate protein/lane) and

16　blotted onto polyvinylidene difluoride (PVDF) membranes. The membranes were blocked for 1 h

17　in TBST (20 mM Tris (pH 7.6), 137 mM NaCl, 0.1 % (w/v) Tween® 20) containing 5 % non-fat

18　dried skimmed milk. Thereafter, blots were incubated with primary antibodies (diluted in TBST

19　containing 5 % BSA) overnight at 4 °C followed by incubation with horseradish peroxidase-

20　conjugated secondary antibodies for 1 h. Proteins were detected using the enhanced

21　chemiluminescence (ECL) reagent (GE Healthcare, Chicago, IL, USA) or Western Lightning Plus-

22　ECL reagents (Perkin Elmer, Waltham, MA, USA). The intensity of bands was quantified by

23　densitometry using the ImageJ software (NIH, Bethesda, MD, US). Phospho- and acetylation-

24　specific signals were normalized to the signal of the respective total proteins. For evaluation of

25　protein expression, the signals were normalized to β-actin.

26

27　*5-Bromo-2'-deoxyuridine (BrdU) proliferation assay*

28　Glyoxal treatment of HUVEC was performed for 24 h in cell culture dishes and, after reseeding,

29　for another 24 h in 24-well plates. Thereafter, cells were starved in starvation medium (M199, 2

30　% FCS, 7.5 U/ml heparin, 680 µM glutamine, 100 U/ml penicillin, 100 µg/ml streptomycin) for 4 h

31　and stimulated with bFGF for 24 h. DNA synthesis was analyzed using the Cell Proliferation

32　ELISA, BrdU (colorimetric) kit from Roche Diagnostics (Mannheim, Germany) according to the

33　manufacturer's protocol. In brief, during the last 5 h of experimental incubation 10 µM BrdU were

34　added. Then, cells were fixed for 30 min in Fix/Denat solution. 200 µl peroxidase-conjugated anti-

1 BrdU-antibody (1:100) were added per well and incubated for 75 min protected from light. Cells

2 were washed three times with PBS before adding 200 µl substrate solution. Reaction was stopped

3 after 5-20 min depending on the color development by adding 50 µl of 1 M H_2SO_4 for 1 min. The

4 solution was transferred into a 96-well plate and absorption was measured at 450 nm.

5

6 *CFSE proliferation assay*

7 HUVEC were washed twice with warm (37°C) HEPES buffer containing 0.25 % human serum

8 albumin (HEPES/HSA) and incubated with 5 µM CFSE for 15 min at 37 °C. After two washing

9 steps with warm HEPES/FCS, cells were incubated with glyoxal in 1 ml experimental medium for

10 the indicated times. Thereafter, cells were washed twice with PBS, detached with 300 µl

11 trypsin/EDTA and transferred to 700 µl of HEPES/FCS. The cell suspension was pooled with 1

12 ml HEPES/FCS obtained after rinsing the dish. 10 ml of HEPES buffer were added and samples

13 centrifuged (500 x g, 1 min). Pellets were resuspended in 300 µl PBS and subjected to flow

14 cytometric analysis. Median values were evaluated using the FlowJo™ software (Becton,

15 Dickinson and Company, Ashland, OR, US).

16

17 *Angiogenesis assay*

18 Glyoxal treatment was performed for 24 h in 90 mm-cell culture dishes and, during generation of

19 spheroids, for another 24 h in 96-well plates. Spheroids were prepared as previously described

20 (Spengler et al., 2018). In brief, cells suspended in growth medium were mixed at a 4:1 ratio with

21 methyl cellulose (12 mg/ml) and 3000 cells/well were cultured in 96-well round-bottom plates for

22 24 h. The formed spheroids were collected, centrifuged (200 x g, 4 min) and washed with HEPES

23 buffer. Then, spheroids were transferred to a fibrinogen solution (1.8 mg/ml in HEPES buffer)

24 containing 20 U/ml aprotinin to obtain a suspension with approximately 100 spheroids per ml. 300

25 µl of this suspension together with 0.2 U thrombin were added per well of a 24-well plate. The

26 plate was incubated for 20 min at 37 °C to allow the formation of a fibrin gel. To equilibrate the

27 gel with medium, M199 containing 2 % FCS, 680 µM glutamine, 100 U/ml penicillin and 100 µg/ml

28 streptomycin was added twice for 15 min. Thereafter, spheroids were cultured in the same

29 medium and stimulated with 50 ng/ml VEGF for 24 h. Finally, spheroids were fixed on ice by

30 adding 1 ml 4 % paraformaldehyde per well for 10 min. After two washing steps with PBS,

31 spheroid sprouting was viewed by light microscopy and pictures were taken (AxioVert 200, Carl

32 Zeiss, Oberkochen, Germany). The number of sprouts was analyzed using cellSens image

33 analysis software (Olympus, Tokyo, Japan).

34

Di Sanzo, Spengler, *et al.*

1   *Cell synchronization with double thymidine block*

2   Cells were synchronized as described previously (Amin and Varma, 2017). Briefly, one day after

3   seeding 2 mM thymidine was added and incubated with cells for 18 h. After washing (twice with

4   PBS, once with M199), cells were cultured in full growth medium for 9 h and subsequently

5   incubated with 2 mM thymidine for another 18 h. Cells were washed as described and glyoxal

6   was added in experimental medium for the indicated times.

7

8   *Cell cycle analysis*

9   During the last 30 min of glyoxal treatment, 10 µM 5-ethynyl-2´-deoxyuridine (EdU) were added

10   to HUVEC cultured on 90 mm-dishes. Cells were washed twice with PBS, detached with 1 ml

11   trypsin/EDTA and transferred to 4 ml of HEPES/FCS. The cell suspension was pooled with 4 ml

12   HEPES/FCS obtained after rinsing the dish and samples were centrifuged. All centrifugations

13   were carried out at 500 x g for 3 min at room temperature if not otherwise stated. Cell pellets were

14   washed once in 1 ml BSA buffer (1 % BSA in PBS), resuspended in 100 µl of the same buffer,

15   fixed with 100 µl of 4 % paraformaldehyde for 15 min, centrifuged and resuspended in 300 µl

16   PBS. 700 µl of 100 % ethanol were added dropwise under constant gentle shaking and samples

17   were frozen overnight. The next day, cells were centrifuged (700 x g, 3 min, RT), washed in 1 ml

18   BSA buffer and permeabilized in 100 µl Triton-based BSA buffer (TBB, 0.2 % Triton X-100 in BSA

19   buffer) for 30 min. Then, cells were centrifuged, resuspended in 500 µl BSA buffer, incubated for

20   1 h, centrifuged again and incubated in 150 µl of primary antibody solution (1:200 p-H3 (S10)

21   antibody in TBB) for 2 h. This was followed by another addition of 500 µl TBB, centrifugation and

22   incubation of cells in 150 µl of secondary antibody solution (1:500 AF488 goat anti-rabbit antibody

23   in TBB) for 1 h. Next, after adding 500 µl TBB, centrifugation and an additional washing with 1 ml

24   BSA buffer, cells were incubated in 100 µl of Click-iT reaction cocktail (2.5 mM $CuSO_4$, 1:200

25   AF647 azide, 50 mM sodium ascorbate in PBS) for 30 min. Subsequently, another washing with

26   1 ml BSA buffer was performed and cells were incubated in 300 µl BSA buffer containing 1 µg

27   DAPI for 30 min. Samples were subjected to flow cytometric analysis with triple detection of

28   AF488, AF647 and DAPI. Percentages of cells in the respective cell cycle phases were evaluated

29   using the FlowJo™ software.

30

31   *Seahorse analysis of cells*

32   HUVEC were seeded into Seahorse XF96 Cell Culture Microplates (3,000 cells/well; Agilent

33   Technologies, Santa Clara, CA, USA), incubated for 24 h and then treated with glyoxal for 48 h.

34   Mito stress test: Medium was replaced with Seahorse XF Base Medium (103334-100, Agilent

1 Technologies, pH adjusted to 7.4), supplemented with 10 mM D-glucose, 2 mM L-glutamine and

2 1 mM sodium pyruvate. Cells were then cultured for another hour in a CO_2-free incubator at 37 °C.

3 Oxygen consumption rates (OCR) and extracellular acidification rates (ECAR) were monitored at

4 basal conditions and after sequential injections of 2 µM oligomycin to block the mitochondrial ATP

5 synthase, 2 µM carbonyl cyanide-4-(trifluoromethoxy)phenylhydrazone (FCCP) to uncouple

6 oxidative phosphorylation and 2 µM antimycin A to fully inhibit mitochondrial respiration.

7 Glycolysis stress test: Medium was replaced with Seahorse XF Base Medium (pH adjusted to 7.4)

8 supplemented with 2 mM L-glutamine, and cells were cultured for another hour in a CO_2-free

9 incubator at 37 °C. OCR and ECAR were monitored at basal conditions and after sequential

10 injections of 10 mM D-glucose, 2 µM oligomycin and 50 mM 2-deoxy-D-glucose, an inhibitor of

11 glycolysis.

12 Measurements in both settings were performed in 3 min mix and 3 min measure cycles at 37 °C

13 in six replicates per condition on a Seahorse XFe96 Analyzer (Agilent Technologies). OCR and

14 ECAR were depicted as pmol/min and mpH/min, respectively, and normalized to the exact cell

15 number of each well measured by high-content microscopy. Wave software (Agilent

16 Technologies) was used to analyze the datasets.

17

18 *High-content microscopy*

19 Cell supernatants were removed from the Seahorse XF96 microplate and cells were fixed for 10

20 min with 100 % methanol at room temperature. Cells were then washed once with PBS and

21 incubated for 10 min with 1 µg/ml DAPI at room temperature. After two more washing steps with

22 PBS, cell nuclei were counted on an ImageXpress Micro confocal high-content imaging system

23 (Molecular Devices, San Jose, CA, USA).

24

25 *ATP measurements*

26 The intracellular ATP content was determined using the ATP Kit SL from Biotherma (Handen,

27 Sweden) according to the manufacturer's protocol. At the end of experimental incubations, cell

28 proteins were denatured by adding 500 µl ethanol per dish. After evaporation of the ethanol,

29 250 µl Tris buffer of the assay kit was added and one freezing/thawing cycle in liquid nitrogen was

30 performed. Cells were then scraped off, centrifuged (700 x g, 5 min) and supernatants subjected

31 to ATP measurements. For normalization, cells in identically treated dishes were lysed with

32 solubilization buffer (100 mM NaOH, 1.9 M Na_2CO_3, 1% SDS) and the protein content was

33 determined according to Lowry.

34

Di Sanzo, Spengler, *et al.*

1 *Intracellular and mitochondrial ROS measurement*

2 30 min before the end of the indicated glyoxal treatment, HUVEC were washed with PBS, 600 µl

3 of the respective staining solution were added, glyoxal was re-added and incubation was

4 completed. The staining solutions contained 5 µM CM-H2DCFDA or 3 µM MitoSOX™ (both

5 Thermo Scientific, MA, Waltham, USA) diluted in HEPES/HSA for the detection of intracellular or

6 mitochondrial ROS, respectively. Cells were washed with PBS, detached with 300 µl

7 trypsin/EDTA and transferred to 700 µl HEPES/FCS. The cell suspension was pooled with 1 ml

8 HEPES/FCS obtained from rinsing the dish, 10 ml HEPES buffer were added and cells

9 centrifuged (500 x g, 1 min). Cell pellets were resuspended in 300 µl PBS and subjected to flow

10 cytometry analysis. Median values were evaluated using the FlowJo™ software.

11

12 *Detection of mitochondrial mass*

13 30 min before the end of the indicated glyoxal treatment HUVEC were washed with PBS and 600

14 µl of 100 nM MitoTracker™ (Thermo Scientific, Waltham, MA, USA) diluted in HEPES/HSA were

15 added. Glyoxal was re-added and incubation was completed. Cells were washed with PBS,

16 detached with 300 µl trypsin/EDTA and transferred to 700 µl HEPES/FCS. The cell suspension

17 was pooled with 1 ml HEPES/FCS obtained from rinsing the dish, 10 ml HEPES/HSA were added

18 and cells centrifuged (500 x g, 1 min). Pellets were resuspended in 300 µl PBS and subjected to

19 flow cytometry analysis. FlowJo™ software was used to evaluate the median values of

20 MitoTracker™-positive cells

21

22 *SA-β-Gal staining*

23 After glyoxal incubation, cells were washed twice with 1 ml cold PBS and fixed with 1 ml of a

24 2 % formaldehyde/0.2 % glutaraldehyde solution for 3 min. SA-β-Gal staining was performed as

25 previously described (Debacq-Chainiaux et al., 2009). Briefly, after two washing steps with PBS,

26 1.5 ml staining solution (40 mM citric acid/Na phosphate buffer, 5 mM $K_4[Fe(CN)_6] \cdot 3H_2O$, 5 mM

27 $K_3[Fe(CN)_6]$, 150 mM NaCl, 2 mM $MgCl_2$, 1:20 X-Gal (20 mg/ml in DMF) in water, pH 6.0) was

28 incubated with cells at 37 °C overnight. Pictures were taken (EVOS™ FL Auto, Thermo Scientific,

29 Waltham, MA, USA) and the number of SA-β-Gal-positive cells was counted using ImageJ and

30 normalized to the total cell number.

31

32 *γH2A.X (S139) immunofluorescence staining*

33 HUVEC were washed with warm (37 °C) HEPES buffer, fixed in ice-cold 4 % paraformaldehyde

34 for 15 min and washed twice with PBS. Cells were permeabilized in PBS containing 0.3 % Triton

Di Sanzo, Spengler, *et al.*

1   X-100 for 5 min. Blocking solution (1 % BSA-C, 5 % goat serum in PBS) was added for 1 h. After

2   two washing steps with PBS, samples were incubated in γH2A.X (S139) antibody diluted in

3   blocking solution (1:400) in a humidified chamber overnight at 4 °C. Cells were washed twice with

4   PBS and incubated with AF488-labelled goat anti-rabbit secondary antibody (1:500 in blocking

5   solution) for 2 h. After two washing steps with PBS, DAPI (1 µg/ml in PBS) was added for 10 min

6   and cells were washed three times with PBS before mounting the coverslips on microscopic slides

7   using Fluoromount-G.

8

9   *α/β-Tubulin and ac-Tubulin (K40) immunofluorescence staining*

10   Washing, fixation and permeabilization of HUVEC were performed as described for γH2A.X

11   (S139) staining. Thereafter, cells were incubated for 2 h with primary antibodies against α/β-

12   tubulin or ac-tubulin (K40) diluted in blocking solution (1:100). After two washing steps with PBS,

13   an AF488-labelled goat anti-rabbit secondary antibody (1:500 in blocking solution) was added for

14   1 h. Cells were washed three times with PBS. Then, DAPI (1 µg/ml in PBS) was added for 10 min

15   and cells were washed three times with PBS before mounting the coverslips on microscopic slides

16   using Fluoromount-G. For immunofluorescence, a LEICA DMi8 TCS SP8 inverted laser scanning

17   microscope was employed (Leica Biosystems, Wetzlar, Germany) and pictures were taken.

18   Evaluation was performed via a blinded approach, in which cells with strongly structured tubulin

19   filaments per high-power field were counted and normalized to the number of DAPI stained nuclei.

20

21   *Data availability*

22   The mass spectrometry proteomics data have been deposited to the ProteomeXchange

23   Consortium via the PRIDE (Perez-Riverol et al., 2019) partner repository with the dataset

24   identifiers:

25

26   TMT-10plex data for organ aging proteome: PXD021883

27   DIA for acetylated peptides: PXD021891

28   MQ searches for CMLpepIP: PXD021921

29   DIA for MEF and HUVEC cells: PXD021985

30

31   In addition, the proteomics data presented in this manuscript are available via a R shiny web

32   server: https://genome.leibniz-fli.de/shiny/orilab/CMLsites/

33

34

Di Sanzo, Spengler, *et al.*

References

Abbas, T., and Dutta, A. (2009). p21 in cancer: intricate networks and multiple activities. Nat Rev Cancer *9*, 400-414.

Ahmad, S., Akhter, F., Shahab, U., Rafi, Z., Khan, M.S., Nabi, R., Khan, M.S., Ahmad, K., Ashraf, J.M., and Moinuddin (2018). Do all roads lead to the Rome? The glycation perspective! Semin Cancer Biol *49*, 9-19.

Amin, M.A., and Varma, D. (2017). Combining Mitotic Cell Synchronization and High Resolution Confocal Microscopy to Study the Role of Multifunctional Cell Cycle Proteins During Mitosis. J Vis Exp.

Ansari, N.A., Chaudhary, D.K., and Dash, D. (2018). Modification of histone by glyoxal: recognition of glycated histone containing advanced glycation adducts by serum antibodies of type 1 diabetes patients. Glycobiology *28*, 207-213.

Avery, N.C., and Bailey, A.J. (2005). Enzymic and non-enzymic cross-linking mechanisms in relation to turnover of collagen: relevance to aging and exercise. Scand J Med Sci Sports *15*, 231-240.

Baldensperger, T., Eggen, M., Kappen, J., Winterhalter, P.R., Pfirrmann, T., and Glomb, M.A. (2020). Comprehensive analysis of posttranslational protein modifications in aging of subcellular compartments. Sci Rep *10*, 7596.

Bao, X., Liu, Z., Zhang, W., Gladysz, K., Fung, Y.M.E., Tian, G., Xiong, Y., Wong, J.W.H., Yuen, K.W.Y., and Li, X.D. (2019). Glutarylation of Histone H4 Lysine 91 Regulates Chromatin Dynamics. Mol Cell *76*, 660-675 e669.

Benjamini, Y., and Hochberg, Y. (1995). Controlling the False Discovery Rate: A Practical and Powerful Approach to Multiple Testing. In Journal of the Royal Statistical Society. Series B (Methodological), pp. 289-300.

Bento, C.F., Marques, F., Fernandes, R., and Pereira, P. (2010). Methylglyoxal alters the function and stability of critical components of the protein quality control. PLoS One *5*, e13007.

Berges, N., Arens, K., Kreusch, V., Fischer, R., and Di Fiore, S. (2017). Toward Discovery of Novel Microtubule Targeting Agents: A SNAP-tag-Based High-Content Screening Assay for the Analysis of Microtubule Dynamics and Cell Cycle Progression. SLAS Discov *22*, 387-398.

Bierhaus, A., Fleming, T., Stoyanov, S., Leffler, A., Babes, A., Neacsu, C., Sauer, S.K., Eberhardt, M., Schnolzer, M., Lasitschka, F., et al. (2012). Methylglyoxal modification of Nav1.8 facilitates nociceptive neuron firing and causes hyperalgesia in diabetic neuropathy. Nat Med *18*, 926-933.

Bilova, T., Paudel, G., Shilyaev, N., Schmidt, R., Brauch, D., Tarakhovskaya, E., Milrud, S., Smolikova, G., Tissier, A., Vogt, T., et al. (2017). Global proteomic analysis of advanced glycation end products in the Arabidopsis proteome provides evidence for age-related glycation hot spots. J Biol Chem *292*, 15758-15776.

Bindea, G., Mlecnik, B., Hackl, H., Charoentong, P., Tosolini, M., Kirilovsky, A., Fridman, W.H., Pages, F., Trajanoski, Z., and Galon, J. (2009). ClueGO: a Cytoscape plug-in to decipher functionally grouped gene ontology and pathway annotation networks. Bioinformatics *25*, 1091-1093.

Bollong, M.J., Lee, G., Coukos, J.S., Yun, H., Zambaldo, C., Chang, J.W., Chin, E.N., Ahmad, I., Chatterjee, A.K., Lairson, L.L., et al. (2018). A metabolite-derived protein modification integrates glycolysis with KEAP1-NRF2 signalling. Nature *562*, 600-604.

Boodhwani, M., and Sellke, F.W. (2009). Therapeutic angiogenesis in diabetes and hypercholesterolemia: influence of oxidative stress. Antioxid Redox Signal *11*, 1945-1959.

Brings, S., Fleming, T., Freichel, M., Muckenthaler, M.U., Herzig, S., and Nawroth, P.P. (2017). Dicarbonyls and Advanced Glycation End-Products in the Development of Diabetic Complications and Targets for Intervention. Int J Mol Sci *18*.

Brosch, M., Yu, L., Hubbard, T., and Choudhary, J. (2009). Accurate and sensitive peptide identification with Mascot Percolator. J Proteome Res *8*, 3176-3181.

Brouhard, G.J., and Rice, L.M. (2018). Microtubule dynamics: an interplay of biochemistry and mechanics. Nat Rev Mol Cell Biol *19*, 451-463.

Brouwers, O., Niessen, P.M., Miyata, T., Ostergaard, J.A., Flyvbjerg, A., Peutz-Kootstra, C.J., Sieber, J., Mundel, P.H., Brownlee, M., Janssen, B.J., et al. (2014). Glyoxalase-1 overexpression reduces endothelial dysfunction and attenuates early renal impairment in a rat model of diabetes. Diabetologia *57*, 224-235.

Brownlee, M. (1995). The pathological implications of protein glycation. Clin Invest Med *18*, 275-281.

Buczak, K., Kirkpatrick, J.M., Truckenmueller, F., Santinha, D., Ferreira, L., Roessler, S., Singer, S., Beck, M., and Ori, A. (2020). Spatially resolved analysis of FFPE tissue proteomes by quantitative mass spectrometry. Nat Protoc *15*, 2956-2979.

Campisi, J., and d'Adda di Fagagna, F. (2007). Cellular senescence: when bad things happen to good cells. Nat Rev Mol Cell Biol *8*, 729-740.

Chaudhuri, J., Bains, Y., Guha, S., Kahn, A., Hall, D., Bose, N., Gugliucci, A., and Kapahi, P. (2018). The Role of Advanced Glycation End Products in Aging and Metabolic Diseases: Bridging Association and Causality. Cell Metab *28*, 337-352.

Chen, L., Cui, Y., Li, B., Weng, J., Wang, W., Zhang, S., Huang, X., Guo, X., and Huang, Q. (2020). Advanced glycation end products induce immature angiogenesis in in vivo and ex vivo mouse models. Am J Physiol Heart Circ Physiol *318*, H519-H533.

Childs, D., Bach, K., Franken, H., Anders, S., Kurzawa, N., Bantscheff, M., Savitski, M.M., and Huber, W. (2019). Nonparametric Analysis of Thermal Proteome Profiles Reveals Novel Drug-binding Proteins. Mol Cell Proteomics *18*, 2506-2515.

Choi, M., Chang, C.Y., Clough, T., Broudy, D., Killeen, T., MacLean, B., and Vitek, O. (2014). MSstats: an R package for statistical analysis of quantitative mass spectrometry-based proteomic experiments. Bioinformatics *30*, 2524-2526.

Ciccia, A., and Elledge, S.J. (2010). The DNA damage response: making it safe to play with knives. Mol Cell *40*, 179-204.

Debacq-Chainiaux, F., Erusalimsky, J.D., Campisi, J., and Toussaint, O. (2009). Protocols to detect senescence-associated beta-galactosidase (SA-betagal) activity, a biomarker of senescent cells in culture and in vivo. Nat Protoc *4*, 1798-1806.

Delgado-Andrade, C. (2016). Carboxymethyl-lysine: thirty years of investigation in the field of AGE formation. Food Funct *7*, 46-57.

Elias, J.E., and Gygi, S.P. (2007). Target-decoy search strategy for increased confidence in large-scale protein identifications by mass spectrometry. Nat Methods *4*, 207-214.

Ferreira, L.T., Figueiredo, A.C., Orr, B., Lopes, D., and Maiato, H. (2018). Dissecting the role of the tubulin code in mitosis. Methods Cell Biol *144*, 33-74.

Fornasiero, E.F., Mandad, S., Wildhagen, H., Alevra, M., Rammner, B., Keihani, S., Opazo, F., Urban, I., Ischebeck, T., Sakib, M.S., et al. (2018). Precisely measured protein lifetimes in the mouse brain reveal differences across tissues and subcellular fractions. Nat Commun *9*, 4230.

Franken, H., Mathieson, T., Childs, D., Sweetman, G.M., Werner, T., Togel, I., Doce, C., Gade, S., Bantscheff, M., Drewes, G., et al. (2015). Thermal proteome profiling for unbiased identification of direct and indirect drug targets using multiplexed quantitative mass spectrometry. Nat Protoc *10*, 1567-1593.

Friguet, B., Bulteau, A.L., Chondrogianni, N., Conconi, M., and Petropoulos, I. (2000). Protein degradation by the proteasome and its implications in aging. Ann N Y Acad Sci *908*, 143-154.

Galligan, J.J., Wepy, J.A., Streeter, M.D., Kingsley, P.J., Mitchener, M.M., Wauchope, O.R., Beavers, W.N., Rose, K.L., Wang, T., Spiegel, D.A., et al. (2018). Methylglyoxal-derived posttranslational arginine modifications are abundant histone marks. Proc Natl Acad Sci U S A *115*, 9228-9233.

Gatto, L., and Lilley, K.S. (2012). MSnbase-an R/Bioconductor package for isobaric tagged mass spectrometry data visualization, processing and quantitation. Bioinformatics *28*, 288-289.

Di Sanzo, Spengler, *et al.*

1 Giacco, F., Du, X., D'Agati, V.D., Milne, R., Sui, G., Geoffrion, M., and Brownlee, M. (2014). Knockdown of
2 glyoxalase 1 mimics diabetic nephropathy in nondiabetic mice. Diabetes *63*, 291-299.
3 Gimbrone, M.A., Jr., and Garcia-Cardena, G. (2016). Endothelial Cell Dysfunction and the Pathobiology of
4 Atherosclerosis. Circ Res *118*, 620-636.
5 Gkogkolou, P., and Bohm, M. (2012). Advanced glycation end products: Key players in skin aging?
6 Dermatoendocrinol *4*, 259-270.
7 Goodson, H.V., and Jonasson, E.M. (2018). Microtubules and Microtubule-Associated Proteins. Cold
8 Spring Harb Perspect Biol *10*.
9 Guedes, S., Vitorino, R., Domingues, M.R., Amado, F., and Domingues, P. (2011). Glycation and oxidation
10 of histones H2B and H1: in vitro study and characterization by mass spectrometry. Anal Bioanal Chem *399*,
11 3529-3539.
12 Hamelin, M., Mary, J., Vostry, M., Friguet, B., and Bakala, H. (2007). Glycation damage targets glutamate
13 dehydrogenase in the rat liver mitochondrial matrix during aging. FEBS J *274*, 5949-5961.
14 Heinze, I., Bens, M., Calzia, E., Holtze, S., Dakhovnik, O., Sahm, A., Kirkpatrick, J.M., Szafranski, K.,
15 Romanov, N., Sama, S.N., et al. (2018). Species comparison of liver proteomes reveals links to naked mole-
16 rat longevity and human aging. BMC Biol *16*, 82.
17 Helton, E.S., and Chen, X. (2007). p53 modulation of the DNA damage response. J Cell Biochem *100*, 883-
18 896.
19 Hipp, M.S., Kasturi, P., and Hartl, F.U. (2019). The proteostasis network and its decline in ageing. Nat Rev
20 Mol Cell Biol *20*, 421-435.
21 Hodges, N.A., Suarez-Martinez, A.D., and Murfee, W.L. (2018). Understanding angiogenesis during aging:
22 opportunities for discoveries and new models. J Appl Physiol (1985) *125*, 1843-1850.
23 Hornbeck, P.V., Zhang. B., and Skrzypek E. (2015). PhosphoSitePlus, 2014: mutations, PTMs and
24 recalibrations. Nucleic Acids Res. *43* (Database issue): D512-20.
25 Jang, J.H., Kim, E.A., Park, H.J., Sung, E.G., Song, I.H., Kim, J.Y., Woo, C.H., Doh, K.O., Kim, K.H., and Lee,
26 T.J. (2017). Methylglyoxal-induced apoptosis is dependent on the suppression of c-FLIPL expression via
27 down-regulation of p65 in endothelial cells. J Cell Mol Med *21*, 2720-2731.
28 Janke, C., and Magiera, M.M. (2020). The tubulin code and its role in controlling microtubule properties
29 and functions. Nat Rev Mol Cell Biol *21*, 307-326.
30 Kelmer Sacramento, E., Kirkpatrick, J.M., Mazzetto, M., Baumgart, M., Bartolome, A., Di Sanzo, S.,
31 Caterino, C., Sanguanini, M., Papaevgeniou, N., Lefaki, M., et al. (2020). Reduced proteasome activity in
32 the aging brain results in ribosome stoichiometry loss and aggregation. Mol Syst Biol *16*, e9596.
33 Kold-Christensen, R., and Johannsen, M. (2020). Methylglyoxal Metabolism and Aging-Related Disease:
34 Moving from Correlation toward Causation. Trends Endocrinol Metab *31*, 81-92.
35 Kuhla, B., Boeck, K., Luth, H.J., Schmidt, A., Weigle, B., Schmitz, M., Ogunlade, V., Munch, G., and Arendt,
36 T. (2006). Age-dependent changes of glyoxalase I expression in human brain. Neurobiol Aging *27*, 815-
37 822.
38 Kuo, L.J., and Yang, L.X. (2008). Gamma-H2AX - a novel biomarker for DNA double-strand breaks. In Vivo
39 *22*, 305-309.
40 Li, P., Chen, D., Cui, Y., Zhang, W., Weng, J., Yu, L., Chen, L., Chen, Z., Su, H., Yu, S., et al. (2018). Src Plays
41 an Important Role in AGE-Induced Endothelial Cell Proliferation, Migration, and Tubulogenesis. Front
42 Physiol *9*, 765.
43 Liao, Y., Wang, J., Jaehnig, E.J., Shi, Z., and Zhang, B. (2019). WebGestalt 2019: gene set analysis toolkit
44 with revamped UIs and APIs. Nucleic Acids Res *47*, W199-W205.
45 Liu, H., Yu, S., Zhang, H., and Xu, J. (2012). Angiogenesis impairment in diabetes: role of methylglyoxal-
46 induced receptor for advanced glycation endproducts, autophagy and vascular endothelial growth factor
47 receptor 2. PLoS One *7*, e46720.

Di Sanzo, Spengler, *et al.*

1 Mathieson, T., Franken, H., Kosinski, J., Kurzawa, N., Zinn, N., Sweetman, G., Poeckel, D., Ratnu, V.S.,
2 Schramm, M., Becher, I., et al. (2018). Systematic analysis of protein turnover in primary cells. Nat
3 Commun *9*, 689.
4 Minguez, P., Letunic, I., Parca, L., Garcia-Alonso, L., Dopazo, J., Huerta-Cepas, J., and Bork, P. (2015).
5 PTMcode v2: a resource for functional associations of post-translational modifications within and
6 between proteins. Nucleic Acids Res *43*, D494-502.
7 Mir, A.R., uddin, M., Alam, K., and Ali, A. (2014). Methylglyoxal mediated conformational changes in
8 histone H2A-generation of carboxyethylated advanced glycation end products. Int J Biol Macromol *69*,
9 260-266.
10 Morcos, M., Du, X., Pfisterer, F., Hutter, H., Sayed, A.A., Thornalley, P., Ahmed, N., Baynes, J., Thorpe, S.,
11 Kukudov, G., et al. (2008). Glyoxalase-1 prevents mitochondrial protein modification and enhances
12 lifespan in Caenorhabditis elegans. Aging Cell *7*, 260-269.
13 Moriya, J., and Minamino, T. (2017). Angiogenesis, Cancer, and Vascular Aging. Front Cardiovasc Med *4*,
14 65.
15 Navarrete Santos, A., Jacobs, K., Simm, A., Glaubitz, N., Horstkorte, R., and Hofmann, B. (2017).
16 Dicarbonyls induce senescence of human vascular endothelial cells. Mech Ageing Dev *166*, 24-32.
17 Nigro, C., Leone, A., Fiory, F., Prevenzano, I., Nicolo, A., Mirra, P., Beguinot, F., and Miele, C. (2019).
18 Dicarbonyl Stress at the Crossroads of Healthy and Unhealthy Aging. Cells *8*.
19 Nigro, C., Leone, A., Raciti, G.A., Longo, M., Mirra, P., Formisano, P., Beguinot, F., and Miele, C. (2017).
20 Methylglyoxal-Glyoxalase 1 Balance: The Root of Vascular Damage. Int J Mol Sci *18*.
21 Okonkwo, U.A., and DiPietro, L.A. (2017). Diabetes and Wound Angiogenesis. Int J Mol Sci *18*.
22 Ori, A., Toyama, B.H., Harris, M.S., Bock, T., Iskar, M., Bork, P., Ingolia, N.T., Hetzer, M.W., and Beck, M.
23 (2015). Integrated Transcriptome and Proteome Analyses Reveal Organ-Specific Proteome Deterioration
24 in Old Rats. Cell Syst *1*, 224-237.
25 Oya-Ito, T., Liu, B.F., and Nagaraj, R.H. (2006). Effect of methylglyoxal modification and phosphorylation
26 on the chaperone and anti-apoptotic properties of heat shock protein 27. J Cell Biochem *99*, 279-291.
27 Perez-Riverol, Y., Csordas, A., Bai, J., Bernal-Llinares, M., Hewapathirana, S., Kundu, D.J., Inuganti, A., Griss,
28 J., Mayer, G., Eisenacher, M., et al. (2019). The PRIDE database and related tools and resources in 2019:
29 improving support for quantification data. Nucleic Acids Res *47*, D442-D450.
30 Pischetsrieder, M., Seidel, W., Munch, G., and Schinzel, R. (1999). N(2)-(1-Carboxyethyl)deoxyguanosine,
31 a nonenzymatic glycation adduct of DNA, induces single-strand breaks and increases mutation
32 frequencies. Biochem Biophys Res Commun *264*, 544-549.
33 Portran, D., Schaedel, L., Xu, Z., Thery, M., and Nachury, M.V. (2017). Tubulin acetylation protects long-
34 lived microtubules against mechanical ageing. Nat Cell Biol *19*, 391-398.
35 Queisser, M.A., Yao, D., Geisler, S., Hammes, H.P., Lochnit, G., Schleicher, E.D., Brownlee, M., and
36 Preissner, K.T. (2010). Hyperglycemia impairs proteasome function by methylglyoxal. Diabetes *59*, 670-
37 678.
38 Rabbani, N., and Thornalley, P.J. (2015). Dicarbonyl stress in cell and tissue dysfunction contributing to
39 ageing and disease. Biochem Biophys Res Commun *458*, 221-226.
40 Ravi, R., Ragavachetty Nagaraj, N., and Subramaniam Rajesh, B. (2020). Effect of advanced glycation end
41 product on paraoxonase 2 expression: Its impact on endoplasmic reticulum stress and inflammation in
42 HUVECs. Life Sci *246*, 117397.
43 Ravichandran, M., Priebe, S., Grigolon, G., Rozanov, L., Groth, M., Laube, B., Guthke, R., Platzer, M., Zarse,
44 K., and Ristow, M. (2018). Impairing L-Threonine Catabolism Promotes Healthspan through Methylglyoxal-
45 Mediated Proteohormesis. Cell Metab *27*, 914-925 e915.
46 Rayess, H., Wang, M.B., and Srivatsan, E.S. (2012). Cellular senescence and tumor suppressor gene p16.
47 Int J Cancer *130*, 1715-1725.

Di Sanzo, Spengler, *et al.*

1 Ritchie, M.E., Phipson, B., Wu, D., Hu, Y., Law, C.W., Shi, W., and Smyth, G.K. (2015). limma powers
2 differential expression analyses for RNA-sequencing and microarray studies. Nucleic Acids Res *43*, e47.
3 Rosca, M.G., Mustata, T.G., Kinter, M.T., Ozdemir, A.M., Kern, T.S., Szweda, L.I., Brownlee, M., Monnier,
4 V.M., and Weiss, M.F. (2005). Glycation of mitochondrial proteins from diabetic rat kidney is associated
5 with excess superoxide formation. Am J Physiol Renal Physiol *289*, F420-430.
6 Ruiz-Meana, M., Minguet, M., Bou-Teen, D., Miro-Casas, E., Castans, C., Castellano, J., Bonzon-Kulichenko,
7 E., Igual, A., Rodriguez-Lecoq, R., Vazquez, J., et al. (2019). Ryanodine Receptor Glycation Favors
8 Mitochondrial Damage in the Senescent Heart. Circulation *139*, 949-964.
9 Sadoul, K., and Khochbin, S. (2016). The growing landscape of tubulin acetylation: lysine 40 and many
10 more. Biochem J *473*, 1859-1868.
11 Saez, I., and Vilchez, D. (2014). The Mechanistic Links Between Proteasome Activity, Aging and Age-related
12 Diseases. Curr Genomics *15*, 38-51.
13 Sanghvi, V.R., Leibold, J., Mina, M., Mohan, P., Berishaj, M., Li, Z., Miele, M.M., Lailler, N., Zhao, C., de
14 Stanchina, E., et al. (2019). The Oncogenic Action of NRF2 Depends on De-glycation by Fructosamine-3-
15 Kinase. Cell *178*, 807-819 e821.
16 Santos, A.L., and Lindner, A.B. (2017). Protein Posttranslational Modifications: Roles in Aging and Age-
17 Related Disease. Oxid Med Cell Longev *2017*, 5716409.
18 Sasaki, M., Kajiya, H., Ozeki, S., Okabe, K., and Ikebe, T. (2014). Reactive oxygen species promotes cellular
19 senescence in normal human epidermal keratinocytes through epigenetic regulation of p16(INK4a.).
20 Biochem Biophys Res Commun *452*, 622-628.
21 Schalkwijk, C.G., van Bezu, J., van der Schors, R.C., Uchida, K., Stehouwer, C.D., and van Hinsbergh, V.W.
22 (2006). Heat-shock protein 27 is a major methylglyoxal-modified protein in endothelial cells. FEBS Lett
23 *580*, 1565-1570.
24 Schindelin, J., Arganda-Carreras, I., Frise, E., Kaynig, V., Longair, M., Pietzsch, T., Preibisch, S., Rueden, C.,
25 Saalfeld, S., Schmid, B., et al. (2012). Fiji: an open-source platform for biological-image analysis. Nat
26 Methods *9*, 676-682.
27 Sena, C.M., Pereira, A.M., and Seica, R. (2013). Endothelial dysfunction - a major mediator of diabetic
28 vascular disease. Biochim Biophys Acta *1832*, 2216-2231.
29 Shaltiel, I.A., Krenning, L., Bruinsma, W., and Medema, R.H. (2015). The same, only different - DNA damage
30 checkpoints and their reversal throughout the cell cycle. J Cell Sci *128*, 607-620.
31 Shapiro, R., McManus, M.J., Zalut, C., and Bunn, H.F. (1980). Sites of nonenzymatic glycosylation of human
32 hemoglobin A. J Biol Chem *255*, 3120-3127.
33 Sharma-Luthra, R., and Kale, R.K. (1994). Age related changes in the activity of the glyoxalase system.
34 Mech Ageing Dev *73*, 39-45.
35 Sliman, S.M., Eubank, T.D., Kotha, S.R., Kuppusamy, M.L., Sherwani, S.I., Butler, E.S., Kuppusamy, P., Roy,
36 S., Marsh, C.B., Stern, D.M., et al. (2010). Hyperglycemic oxoaldehyde, glyoxal, causes barrier dysfunction,
37 cytoskeletal alterations, and inhibition of angiogenesis in vascular endothelial cells: aminoguanidine
38 protection. Mol Cell Biochem *333*, 9-26.
39 Smuda, M., Henning, C., Raghavan, C.T., Johar, K., Vasavada, A.R., Nagaraj, R.H., and Glomb, M.A. (2015).
40 Comprehensive analysis of maillard protein modifications in human lenses: effect of age and cataract.
41 Biochemistry *54*, 2500-2507.
42 Snow, L.M., Fugere, N.A., and Thompson, L.V. (2007). Advanced glycation end-product accumulation and
43 associated protein modification in type II skeletal muscle with aging. J Gerontol A Biol Sci Med Sci *62*,
44 1204-1210.
45 Song, Y., and Brady, S.T. (2015). Post-translational modifications of tubulin: pathways to functional
46 diversity of microtubules. Trends Cell Biol *25*, 125-136.
47 Spengler, K., Grosse, S., Kryeziu, N., Knierim, A., and Heller, R. (2018). Studying the Role of AMPK in
48 Angiogenesis. Methods Mol Biol *1732*, 519-537.

Di Sanzo, Spengler, *et al.*

1 Spengler, K., Kryeziu, N., Grosse, S., Mosig, A.S., and Heller, R. (2020). VEGF Triggers Transient Induction
2 of Autophagy in Endothelial Cells via AMPKalpha1. Cells *9*.
3 Sudnitsyna, M.V., and Gusev, N.B. (2017). Methylglyoxal and Small Heat Shock Proteins. Biochemistry
4 (Mosc) *82*, 751-759.
5 Sun, L., Bai, Y., and Du, G. (2009). Endothelial dysfunction--an obstacle of therapeutic angiogenesis. Ageing
6 Res Rev *8*, 306-313.
7 Takahashi, A., Ohtani, N., Yamakoshi, K., Iida, S., Tahara, H., Nakayama, K., Nakayama, K.I., Ide, T., Saya,
8 H., and Hara, E. (2006). Mitogenic signalling and the p16INK4a-Rb pathway cooperate to enforce
9 irreversible cellular senescence. Nat Cell Biol *8*, 1291-1297.
10 Teissier, T., and Boulanger, E. (2019). The receptor for advanced glycation end-products (RAGE) is an
11 important pattern recognition receptor (PRR) for inflammaging. Biogerontology *20*, 279-301.
12 Thornalley, P.J. (2008). Protein and nucleotide damage by glyoxal and methylglyoxal in physiological
13 systems--role in ageing and disease. Drug Metabol Drug Interact *23*, 125-150.
14 Verzijl, N., DeGroot, J., Oldehinkel, E., Bank, R.A., Thorpe, S.R., Baynes, J.W., Bayliss, M.T., Bijlsma, J.W.,
15 Lafeber, F.P., and Tekoppele, J.M. (2000). Age-related accumulation of Maillard reaction products in
16 human articular cartilage collagen. Biochem J *350 Pt 2*, 381-387.
17 Wang, H., Liu, J., and Wu, L. (2009). Methylglyoxal-induced mitochondrial dysfunction in vascular smooth
18 muscle cells. Biochem Pharmacol *77*, 1709-1716.
19 Wang, Y., Hall, L.M., Kujawa, M., Li, H., Zhang, X., O'Meara, M., Ichinose, T., and Wang, J.M. (2019).
20 Methylglyoxal triggers human aortic endothelial cell dysfunction via modulation of the KATP/MAPK
21 pathway. Am J Physiol Cell Physiol *317*, C68-C81.
22 Wang, Y., Yu, Y., Li, G.B., Li, S.A., Wu, C., Gigant, B., Qin, W., Chen, H., Wu, Y., Chen, Q., et al. (2017).
23 Mechanism of microtubule stabilization by taccalonolide AJ. Nat Commun *8*, 15787.
24 Waris, S., Winklhofer-Roob, B.M., Roob, J.M., Fuchs, S., Sourij, H., Rabbani, N., and Thornalley, P.J. (2015).
25 Increased DNA dicarbonyl glycation and oxidation markers in patients with type 2 diabetes and link to
26 diabetic nephropathy. J Diabetes Res *2015*, 915486.
27 Xu, Z., Schaedel, L., Portran, D., Aguilar, A., Gaillard, J., Marinkovich, M.P., Thery, M., and Nachury, M.V.
28 (2017). Microtubules acquire resistance from mechanical breakage through intralumenal acetylation.
29 Science *356*, 328-332.
30 Yamawaki, H., and Hara, Y. (2008). Glyoxal causes inflammatory injury in human vascular endothelial cells.
31 Biochem Biophys Res Commun *369*, 1155-1159.
32 Ye, J., Ai, X., Eugeni, E.E., Zhang, L., Carpenter, L.R., Jelinek, M.A., Freitas, M.A., and Parthun, M.R. (2005).
33 Histone H4 lysine 91 acetylation a core domain modification associated with chromatin assembly. Mol
34 Cell *18*, 123-130.
35 Zemva, J., Fink, C.A., Fleming, T.H., Schmidt, L., Loft, A., Herzig, S., Kniess, R.A., Mayer, M., Bukau, B.,
36 Nawroth, P.P., et al. (2017). Hormesis enables cells to handle accumulating toxic metabolites during
37 increased energy flux. Redox Biol *13*, 674-686.
38 Zhang, Y., and Hunter, T. (2014). Roles of Chk1 in cell biology and cancer therapy. Int J Cancer *134*, 1013-
39 1023.
40 Zheng, Q., Omans, N.D., Leicher, R., Osunsade, A., Agustinus, A.S., Finkin-Groner, E., D'Ambrosio, H., Liu,
41 B., Chandarlapaty, S., Liu, S., et al. (2019). Reversible histone glycation is associated with disease-related
42 changes in chromatin architecture. Nat Commun *10*, 1289.
43 Zheng, Q., Osunsade, A., and David, Y. (2020). Protein arginine deiminase 4 antagonizes methylglyoxal-
44 induced histone glycation. Nat Commun *11*, 3241.

45